Modeling and predicting oceanic drifts of plastic waste with physical and data-driven approaches.

Manon Béchaz

and under the supervision of

Devis Tuia[1]
Emanuele Dalsasso[1]
Marc Rußwurm[2]

[1]École Polytechnique Fédérale de Lausanne (EPFL), Environmental Computational Science and Earth Observation Laboratory
[2]Wageningen University

19 January 2024

This work has been realized in the
Environmental Computational Science and Earth Observation Laboratory, EPFL

Abstract

Predicting oceanic drifts of plastic waste in oceans is a pressing environmental challenge, posing a severe threat to marine ecosystems and raising important public health concerns. This thesis addresses this issue by exploring different methodologies for predicting oceanic drifts of plastic waste. Particularly, faced with the challenges posed by the tested traditional physical modeling approaches, this work explores the potential of data-driven methods as a complementary solution. Acknowledging the limitations of standalone data-driven and physical approaches, the thesis establishes comprehensive baseline models integrating both physical and data-driven components, with the goal of demonstrating the efficiency of hybrid approaches.

The physical model, while demonstrating satisfactory results, encounters difficulties in predicting trajectories near coastal regions. The integration of a data-driven correction term significantly enhances the accuracy of the predictions, overcoming the limitations imposed by coarse environmental data resolution. Proposed further improvements include extending the spatial and temporal context for predictions and incorporating trajectory information into the model structure. Augmenting data with historical positions and past environmental context proves beneficial, substantially improving prediction accuracy.

Despite the remaining challenges, the study underscores the potential efficacy of hybrid models in predicting the drift of floating objects. The combination of physical and data-driven approaches holds promise for addressing the intricate dynamics of floating object trajectories, contributing to effective plastic pollution mitigation. The findings contribute to ongoing efforts in environmental conservation and advocate for the adoption of hybrid methodologies in addressing complex challenges in oceanic plastic waste management.

Résumé

La prédiction de la dérive des objets flottants, et notamment du plastique dans les océans est un défi environmental majeur de nos jours, ce plastique représentant une menace grandissante aussi bien pour les écosystèmes marins que pour la santé publique. Ce projet aborde cette question en explorant différentes méthodologies pour prédire les dérives océaniques des déchets plastiques. En particulier, face aux défis posés par les approches traditionnelles de modélisation physique, ce travail explore le potentiel de méthodes basées sur les données et les récentes avancées en deep learning. Reconnaissant les limites des deux approches, ce projet établit notamment des modèles de référence hybrides à la frontière des deux démarches.

Le modèle physique seul, tout en démontrant des résultats satisfaisants, rencontre des difficultés dans la prédiction des trajectoires près des côtes. L'intégration d'un terme de correction basé sur un modèle de deep learning améliore considérablement la précision des prédictions, malgré quelques limites imposées par la résolution grossière des données environnementales. Des améliorations supplémentaires sont proposées, comprenant l'extension du contexte spatial et temporel utilisé pour les prédictions et l'ajout de la notion de trajectoire dans la structure du modèle. En particulier, l'addition de données spatiales et temporelles de positions antérieures de l'objet s'avère bénéfique et améliore considérablement la précision des prédictions.

Malgré les difficultés qui subsistent, ce projet souligne l'efficacité potentielle des modèles hybrides pour prédire la dérive des objets flottants. La combinaison d'approches physiques et deep learning est prometteuse pour traiter la dynamique complexe des trajectoires des objets flottants, contribuant ainsi à une atténuation efficace de la pollution plastique. Les résultats obtenus participent activement aux efforts actuels de conservation de l'environnement et plaident en faveur de l'adoption de méthodologies hybrides pour relever les défis complexes de la gestion des déchets plastiques océaniques.

Contents

Introduction

The growing proliferation of plastic waste in oceans constitutes an important and intricate environmental challenge, demanding urgent attention and innovative solutions. The exponential increase in plastic production and consumption over the past few decades, coupled with inadequate waste management infrastructure, has led to a proliferation of plastic debris within marine ecosystems. Recent statistics underscore the gravity of this issue [1], revealing that millions of tons of plastic enter oceans annually, contributing to expansive floating debris fields accumulating in various marine habitats. Beyond the aesthetic degradation of coastlines, plastic pollution poses profound threats to marine biodiversity, with destructive consequences for ecosystems and the species they support [2]. Furthermore, the persistence of plastic in the marine environment also engenders socio-economic and public health challenges [3], raising concerns about the potential transfer of contaminants up the food chain [4]. Consequently, understanding and modeling the physics governing the drift of floating objects is not only of scientific interest but also has profound implications for environmental conservation and human societies.

The prediction of oceanic drifts of plastic waste, ranging from tiny particles of microplastics to massive cargo containers lost at sea [5][6] poses formidable challenges. The interplay of complex physical factors, such as currents, wind patterns, and temperature gradients [7][8], poses a considerable bottleneck to the accurate modeling of plastic trajectories [9]. The ocean's dynamic nature, marked by turbulence and variability on both temporal and spatial scales, associated with the complex interactions between the ocean and the atmosphere, renders traditional modeling approaches susceptible to strong inaccuracies [10]. Capturing these dynamics demands sophisticated modeling frameworks that must in addition cope with the unpredictability of environmental variables.

Given these numerous challenges inherent in predicting oceanic drifts of plastic waste through traditional physical modeling, recent successes in data-driven approaches for environmental modeling present an appealing alternative to explore [11][12]. Data-driven approaches, leveraging machine learning algorithms and statistical analyses, have demonstrated efficiency in capturing complex and nonlinear environmental processes. By making the most out of the wealth of available environmental data, including satellite observations, oceanographic measurements, and meteorological records, they offer a promising path to enhance the accuracy of predictions [13][14][15][16].

While data-driven approaches exhibit considerable promise in environmental modeling, their standalone utilization may however be limited by challenges such as interpretability and the potential emergence of unphysical solutions lacking grounding in established physical principles. In the context of predicting oceanic drifts of plastic waste, these limitations highlight the importance of considering hybrid approaches that integrate both physical understanding and data-driven techniques to harness the strengths of both methods [17].

This thesis has therefore two primary objectives. Firstly, it aims to establish comprehensive baseline models for plastic drift prediction, integrating both physical and data-driven components. Secondly,

it aspires to constitute a "proof of concept" for the efficiency of hybrid approaches in plastic drift prediction. The novelty of this hybrid methodology lies in its ability to combine the interpretability of physical models with the data-driven capacity to capture the complexity of drift dynamics.

The rest of this work is structured in the following way: Section 1 introduces the physics behind the drift of a floating object and previous related work. Section 2 gives an overview of the data and its preprocessing. Section 3 explains the model used. The experimental setup is extensively described in Section 4 and the results are provided in Section 5. The latter are eventually discussed in Section 6.

1   Related Work

In this first section, we begin by outlining the fundamental principles of physics underlying the drift of floating objects, before providing an overview of existing research on its numerical simulation.

1.1   The physics behind the drift of floating objects

A first step towards the modeling and prediction of the movement of floating objects in the ocean is the understanding of the fundamental principles behind their motion. From phytoplankton and tiny particles of microplastic to massive cargo containers, there are numerous drifting objects in the ocean. They are usually separated into two categories: (larger or smaller) floating objects and oil spills. We will in this work only consider the first scenario. For the second case, the interested reader may find additional information in the following articles [6][10][18][19].

Numerous factors drive the surface ocean circulation, which is typically broken down into different current components, such as the ocean surface currents, the wind drift, the wave-induced Stokes drift, and the geostrophic currents.

1.1.1   Ocean surface currents

The first and most important factor in the movement of floating objects is the ocean surface current. Near the surface, the latter is mostly driven by wind, but the Coriolis force as well as the interior pressure field (pressure gradient) are also important forces to consider. The combination of these forces gives rise to different physical phenomena, described in the following paragraphs, whose influence on the movement of objects on the surface is far from negligible. The mathematical details are provided in Appendix A. Note that the tidal forces as well as the deep ocean currents have a minor influence on the drift of floating objects.

The Ekman currents   The Ekman spiral results from a force balance between the wind shear stress force, the Coriolis force and the water drag. While the wind forcing induces a frictional drag on the surface and a movement of the upper layer of the ocean in the direction of the wind (each thin layer dragging the layer beneath it), the Coriolis force modifies the direction of the current. The water is deflected to the right of the wind direction in the Nothern Hemisphere and to the left in the Southern Hemisphere. As a consequence, each layer of water put into motion by the layer above slightly shifts direction, resulting in a change in the direction of water with increasing depth, creating the so-called Ekman spiral, depicted in Figure 1a. As a result, the movements of floating objects in response to the wind are not parallel to the wind but at an angle of 20° - 40° to the right or left of it. The created current is about 2% of the wind speed.

Inertial currents   When no wind forcing term is applied, the Coriolis force still impacts the dynamics of the upper layer of the ocean. For already moving ocean particles (take for example the case of wind blowing for some time before stopping), the Coriolis force, perpendicular to the path of the parcels, induces once again a constant change of direction and the parcels move on a circle, as shown in Figure 1b. Inertial currents are the most common currents in the oceans.

(a)   (b)
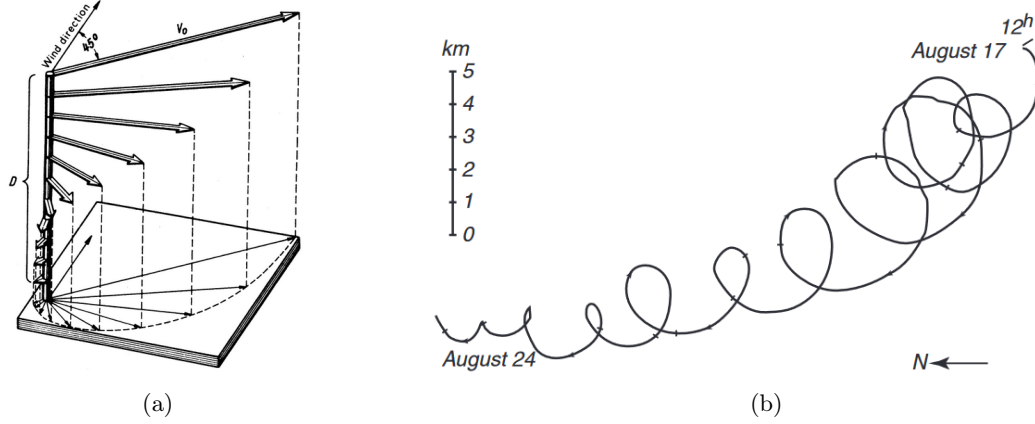
Figure 1: (a) Ekman spiral. Each layer of water in motion slightly shifts direction with respect to the previous layer as a result of the Coriolis force. (b) Consequence of the inertial current on the trajectory of a water parcel. Both illustrations are taken from the Introduction To Physical Oceanography by Robert H. Stewart [7].

Geostrophic currents   The geostrophic currents, induced by inner pressure gradients, are long-term patterns that integrate conditions over month to year. The pressure gradients are of two types. The increase in pressure with depth obviously gives rise to vertical pressure gradients, and hence vertical currents, but since the ocean surface is never perfectly flat, we also observe horizontal pressure variations at a given depth h, and hence horizontal currents that influence the drift of floating objects.

1.1.2   Water drag versus Wind drag

While the wind indirectly influences the drift of floating objects through the role it plays in the formation of ocean surface currents, it also has a significant direct influence on their movement, especially when those objects are not entirely submerged [6]. Wind-forced drift is frequently referred to as leeway drift, sometimes also known as windage.

By balancing the drag forces associated with the wind and ocean currents resulting from the phenomena described in Section 1.1.1, we can derive an expression for the velocity $\boldsymbol{v}$ of a floating object at the surface as a function of the wind speed and surface current, $\boldsymbol{v}_W$ and $\boldsymbol{v}_O$ respectively. More

precisely, the latter is given by

$$\boldsymbol{v} = \boldsymbol{v}_W + \underbrace{\sqrt{\frac{\rho_A C_A A_A}{\rho_W C_W A_W}}}_{\alpha} \boldsymbol{v}_A, \tag{1}$$

with ρ_W, ρ_A the density of water and air, C_W, C_A drag coefficients for water and air, and A_W, A_A the cross-sectional surface areas of the object facing the relative flow of the water and air. The derivation is provided in Appendix A.4.

For a thin horizontally floating object, which has equal areas of the surface exposed to seawater and air, α becomes the Nansen number defined in [20] : $N_a = \sqrt{\frac{\rho_A C_A}{\rho_W C_W}}$. In many cases the air and water drag coefficients can be considered approximately equal, leading to a wind factor $\alpha \approx \sqrt{\rho_A/\rho_W} \approx 3\%$ [21].

This equation provides us with a simple approximation of the drift velocity of a floating object and will serve as a basis for the numerical modeling of drift trajectories.

1.1.3   Influence of the Waves and Stokes drift

Despite their periodic motion, surface waves also generate a net drift in the direction of wave propagation known as the Stokes drift. With the exception of a few simplified analytical scenarios, the exact derivation and computation of the Stokes drift is far from trivial and requires the use of either Lagrangian equations [22] or a Taylor series expansion in a two-dimensional wave field [23]. Stokes [23], Chang [22], Longuet-Higgins [24] and Huang [25] also derived analytical solutions for single waves, shallow waters, and random wave fields respectively. For the interested reader, a more in-depth review of progress in fundamental and applied research on Stokes drift was made by T. S. van den Bremer and Ø. Breivik [26].

1.2   Numerical modeling of oceanic drift

The prediction of surface ocean drift for floating objects has gained increasing attention from researchers in recent years. Beyond the technical complexities associated with replicating and forecasting intricate and turbulent behaviors, the precise prediction of floating object movements holds significant implications for various applications. These applications span a range of domains, including search and rescue operations [14], ship trajectory prediction [13], icebergs monitoring [21], and oil spill prediction [10][19][27].

1.2.1   Physical models for oceanic drift prediction

A frequently adopted approach for predicting the drift of floating objects assumes the drift velocity to be a linear combination of velocity terms associated with specific processes, including the surface

current, the wind velocity, the wind drag, and the waves. The majority of developed models are therefore built upon the physical principles outlined in Section 1.1, and when the wave-induced drift is not explicitly considered, equation (1) is commonly utilized as a groundwork. The model derived from this equation is expressed by the following widely used equation:

$$\boldsymbol{u}_d = \boldsymbol{u}_O + \alpha \boldsymbol{u}_W, \tag{2}$$

where $\boldsymbol{u}_O$ represents the ocean surface current, $\boldsymbol{u}_W$ is the wind velocity, and α is a wind drift factor empirically determined. This fundamental approach results in the drift velocity of a floating object being characterized as the near-surface ocean current velocity combined with a small percentage of the wind velocity above the surface, and serves as the baseline model in numerous studies [10][27][28][29][30][31].

The necessity to account for waves and the wave-induced Stokes drift remains a subject of ongoing debate. In many cases, wave effects are fully parameterized using only wind speed and direction, assuming a constant correlation between waves and wind [28]. However, recent efforts have been directed towards explicitly considering wave effects. Notable works in this regard include the contributions of Rohrs et al. [32], which addresses the effects of surface waves on ocean currents and drifter trajectories, and Onink et al. [9], examining the role of Stokes Drift in the accumulation of floating microplastics. Additionally, research by Bosi et al. [5], Tamtare et al. [31] and Callies et al. [29] also contributes to the ongoing discussion on this topic.

In recent years, several large Lagrangian numerical frameworks, based on the aforementioned approach, have been developed. Notable examples include COZOIL [33], GULFSPILL [19], MEDSLIK [34][35], and OILTRANS [36], which are dedicated to oil spills modeling. Additionally, frameworks such as Ariane [37] and TRACMASS [38]) have been established to calculate the trajectories of individual particles. More recently, the introduction of Parcels ('Probably A Really Computationally Efficient Lagrangian Simulator') [39][40] has contributed to scalability and high performance within the Lagrangian modeling framework.

These studies and frameworks served as foundational elements for more extensive investigations. Noteworthy among them is the work of Lebreton et al. [41], which delves into the examination of the transport and accumulation of floating debris on a global scale. This study employs a global ocean circulation model coupled with a Lagrangian particle tracking model, building upon the established frameworks and methodologies in the field.

1.2.2   Data-driven approaches for oceanic drift predictions

Along with these purely physical approaches, the recent advancements in machine learning coupled with the increasing computational capabilities have led to a growing interest in employing data-driven methods for predicting oceanographic phenomena and the drift of floating objects.

In particular, Long Short-Term Memory (LSTM) networks, recognized for their capacity to handle

sequential data and capture temporal dependencies, have been increasingly employed in oceanic predictions. Liu et al. for instance demonstrated the efficacy of LSTM in predicting ocean-temperature changes [42]. Similarly, Choi et al. leveraged LSTM to forecast occurrences of abnormally high water temperature phenomena [43]. Expanding the scope to collision avoidance strategies, Park et al. [44] proposed a marine collision avoidance algorithm, where the ship trajectory prediction model was developed using bidirectional LSTM. Eventually, Li et al. [14] coupled LSTM with with dense neural network (LSTM-DNN) to calculate marine drifting trajectory, drastically improving the accuracy of drifting trajectory compared with a conventional LSTM-based prediction model. With the same idea of counterbalancing the LSTM with other deep learning approaches, Botvynko et al [15] developed the DriftNet, an architecture combining LSTM with a convolutional architecture with a spatially latent representation to forecast drift processes.

These examples underscore the performance of data-driven methods in diverse oceanic prediction scenarios, offering valuable insights into their potential contributions to understanding and mitigating various environmental challenges, in particular in the case of oceanic drift prediction.

1.2.3   Hybrid approaches for oceanic drift predictions

Given the inherent limitations of machine and deep learning approaches, notably their reduced interpretability and limited physical understanding, hybrid algorithms, combining the strengths of both approaches, have also recently emerged for environmental forecasting.

For example, in the context of sea surface temperature prediction, de Bézenac et al. [45] introduced a Convolutional–Deconvolutional (CDNN) module. This module is designed to predict a motion field, which is then integrated to obtain a future temperature map, thus replacing the traditional approach and the direct prediction of future temperature using a neural network. Adopting a different perspective, Shen et al. [16] constructed a neural network based on a convolutional neural network (UNet) and Gated Recurrent Unit (GRU), trained to rectify float trajectories derived from a physics-based ocean model. Similarly, Yin et al. [46] proposed the APHYNITY model, augmenting an ordinary differential equation (ODE) solver with an additive correction predicted by a data-driven counterpart.

Despite their relatively nascent exploration in the realm of oceanic predictions, these methodologies exhibit significant promise, offering novel perspectives and strategies for addressing the interpretability and physical understanding challenges inherent in traditional machine and deep learning approaches.

2 Data

2.1 Drifters trajectories

Two sets of tracks of GPS surface drifters have been used in this work:

- **Dataset 1** [47] This dataset, compiled by Tamtare et al. comprises a collection of drifting buoy trajectories. The buoys were deployed in various locations in the Estuary and Gulf of St. Lawrence, Canada in June-July and August-November 2014 and 2015. The drifting buoys are constructed with a 4 cm-thick plate measuring 25-40 cm in diameter, equipped with a GPS tracking device that records its location every 10 minutes. To prevent capsizing in wavy conditions, a 1 kg weight is hanging 20 cm below the plate.

- **Dataset 2** [48] The second dataset is a dataset of sea surface temperature generated from the temperature observations at regular hourly time steps of surface drifting buoys within NOAA's Global Drifter Program. For our analysis, we focus on extracting buoy trajectories, omitting the associated temperature data. This dataset provides extensive spatial and temporal coverage, spanning the years 1989 to 2020 and encompassing nearly the entire Earth's submerged surface, totaling 17324 trajectories. The drifters within the dataset exhibit variable sizes and geometries, with some featuring a 'drogue' or sea anchor positioned at a depth of 15 meters.

A comparative analysis of the two datasets is presented in Table 1. Visualization of the datasets is available in Figures 2 and 3.

Property	Dataset 1	Dataset 2
Number of trajectories	103	17324
Number of points	17108	166M
Length of the trajectories	Between a few days and a few weeks	Up to a few months
Geographical area	Estuary and Gult of St. Lawrence	All around the world
Date	2014-2015, June-November	1989-2020, all months
Frequency of observation	every 10 min	every 1h

Table 1: Main properties of the two datasets of drifters trajectories.

2.2 Environmental data

Oceanic surface current velocities are provided by the HYbrid Coordinate Ocean Model or HYCOM [49]. The model possesses a resolution of $0.08° \times 0.08°$ between 40S-40N, and $0.08° \times 0.04°$ poleward of 40S/40N. It has a 3 hourly temporal frequency, and data is available from 2014 onwards. More details on the HYCOM model can be found in [50].
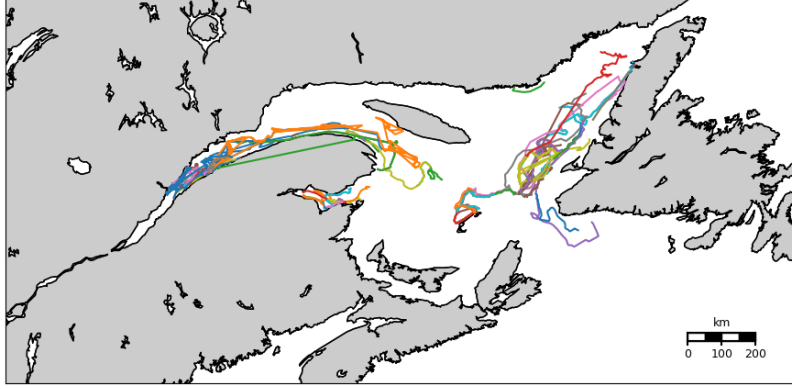
Figure 2: Dataset 1. Geographical positions reported by drifting buoys. Each colored line corresponds to the trajectory of a drifting buoy.
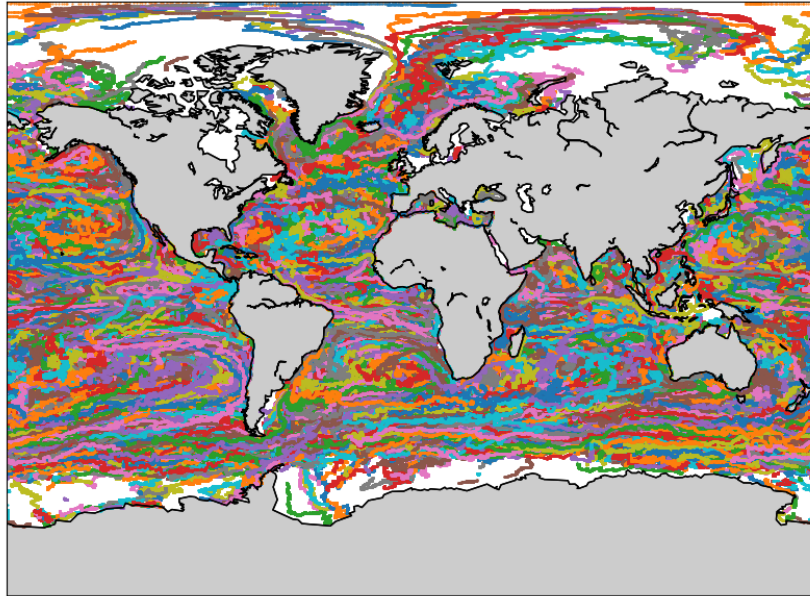
Figure 3: Dataset 2. Geographical positions reported by drifting buoys. Each colored line corresponds to the trajectory of a drifting buoy.

Atmospheric and ocean-wave quantities are for their part obtained from ECMWF's ERA5 model [51]. We are in particular interested in the wind velocity near the surface, approximated by ERA5's 10-m wind vectors, as well as the surface Stokes drift. Data is available from 1940 onwards. The model has a spatial resolution of $0.25° \times 0.25°$ for atmospheric quantities and $0.5° \times 0.5°$ for ocean waves, and an hourly temporal frequency.

Typical vector fields obtained are provided in Figure 4.
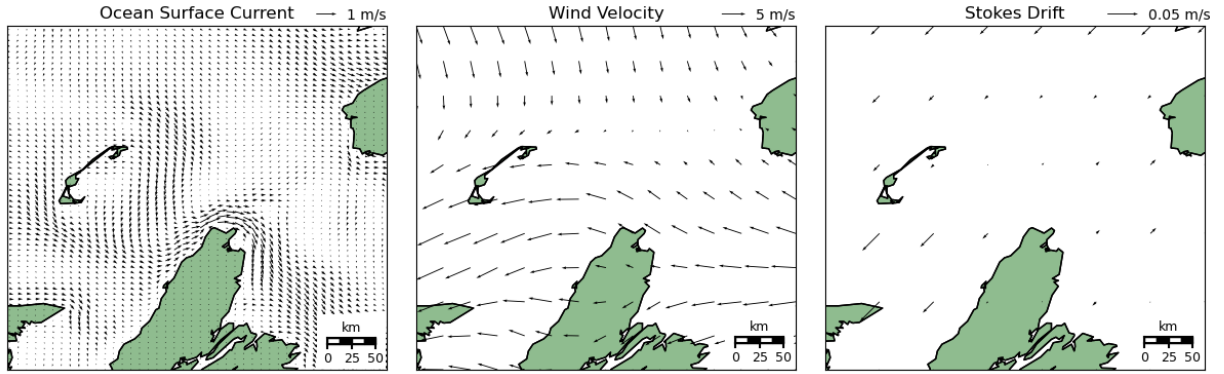
Figure 4: Example of typical ocean surface current, wind velocity and Stokes drift vector fields.

2.3 Interpolation of the environmental data

Because the environmental data (surface current and wind velocities, Stokes drift) are defined on a discrete grid only, a pre-processing procedure is needed to reconstruct the vector fields at any given point. The data being defined on a regular grid, we conducted linear interpolation using `Scipy`'s `RegularGridInterpolator`. This process enables us to acquire values for the winds and currents at any given object position within the study area. The result of this interpolation for the wind field is shown in Figure 5.
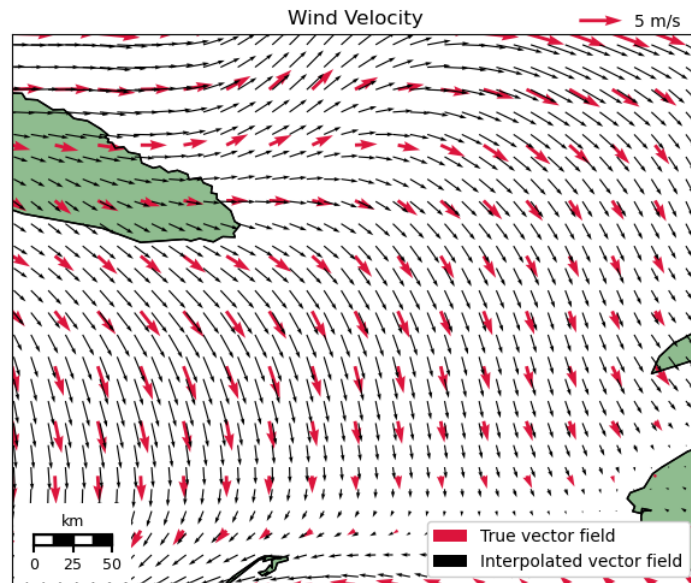
Figure 5: Results of the interpolation procedure for the wind field: in red the original velocity field and in black the interpolated one. The interpolated vector field has a resolution of $0.12° \times 0.12°$ in this example, against $0.25° \times 0.25°$ for the original wind field.

3   Model

We introduce in this work a hybrid model characterized by the integration of a physics-based component and a data-driven counterpart. This approach combines the strengths of physics-based principles and machine learning techniques, hoping to enhance the overall robustness and predictive capabilities of our model.

The model, depicted in Figure 6 aims at predicting the position of the floating object, based on its initial position and additional information on the current, waves and wind field surrounding it. Given the initial position at time t, the model predicts a single position at time $t + 1\text{h}$. The entire trajectory is obtained by successively running the model on obtained positions.

The model consists of a physical module that predicts the future position based on a linear model, and a data-driven component trained to predict a correction to this prediction. The final forecast of the model is taken as the sum of the physical model prediction and the correction predicted by the data-driven component. Each of these blocks is described in more detail in the following sections.
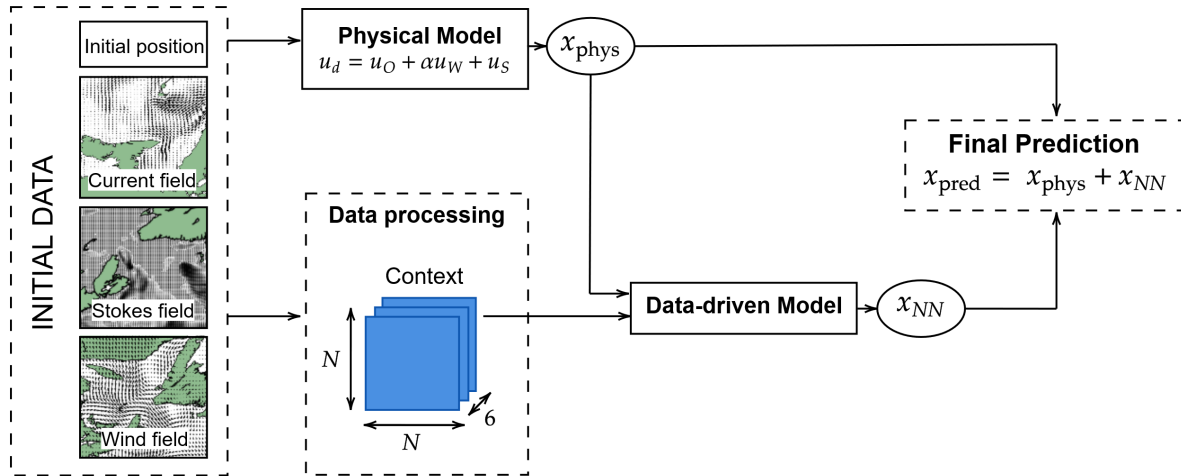
Figure 6: Structure of the proposed hybrid model architecture. A physical model, described in section 3.1 produces a first prediction based on the initial position and the current and wind fields surrounding the object. In parallel, the initial data are fed to a data processing pipeline that extracts the context around the object (see section 3.2.1). Using this context and the physical prediction, a final data-driven part, illustrated in Figure 9 and Section 3.2 outputs a correction to this prediction. The final forecast is taken as the sum of the physical prediction and the correction.

16

3.1   Physical model

3.1.1   Model

The physical model uses a quite intuitive way of describing the movement of an object at the surface of the ocean and considers the latter to be partially driven by the current on the surface of the water and partially, if part of it is emerged, by the wind, thus following the approach commonly adopted in the literature (see Section 1.2.1). As described in this section, this approach leads to the following estimation for the drift velocity of a floating object:

$$\boldsymbol{u}_d = \boldsymbol{u}_O + \alpha \boldsymbol{u}_W, \tag{3}$$

with the ocean surface motion $\boldsymbol{u}_O$ taken from the interpolated values provided by the HYCOM dataset and accounting for all the phenomena influencing the dynamics of the upper part of the ocean, whether it be the Ekman currents, the geostrophic or the tidal currents; $\boldsymbol{u}_W$ the wind velocity obtained from ERA5 data, and α a wind drift factor.

Note that we would ideally need the values of the ocean surface current and at the surface. In practice however, many ocean and weather prediction models do not resolve the marine atmospheric boundary layer. In most cases the surface current velocity is therefore taken from the top cell of the ocean circulation model and the wind velocity from the bottom cell of the whether prediction model, usually at 10m above sea surface. Such approximations inevitably result in more or less significant errors, as highlighted by Callies et al. [29] and Tamtare et al. [30].

In equation 3, the wind factor is assumed to be scalar, i.e. that the movement of a floating object in response to the wind is parallel to the wind. However, as described in section 1.1 the Coriolis force leads to a non-negligible deflection that must be taken into account. In previous work [18][19][34], this was done by adding a drift angle θ to the drift factor, leading to the following parametrization:

$$\boldsymbol{u}_d = \boldsymbol{u}_O + \boldsymbol{A}\boldsymbol{u}_W, \qquad \textbf{(Model A)} \tag{4}$$

with

$$\boldsymbol{A} = \alpha \begin{pmatrix} \cos\theta & \sin\theta \\ -\sin\theta & \cos\theta \end{pmatrix}. \tag{5}$$

3.1.2   Stokes drift

As discussed in Section 1.2.1, whether or not Stokes drift should be explicitly included in numerical models is still a matter of debate. Starting from the model in equation (4), Stokes drift can be accounted for by adding its value $\boldsymbol{u}_S$ obtained from a spectral wave model (Here ERA5 wave data). However, there are two distinct approaches to the addition of Stokes drift. Since the latter is somewhat correlated with the wind, we can first consider Stokes drift and wind drag as alternatives, the addition of one meaning the deletion of the other. Conversely, an alternative perspective asserts

that, despite their correlation, these two terms provide complementary contributions, both of which are indispensable for trajectory prediction. Depending on the perspective adopted, the following two models are derived:

$$\boldsymbol{u}_d = \boldsymbol{u}_O + \boldsymbol{u}_S, \qquad \textbf{(Model B)} \qquad (6)$$

$$\boldsymbol{u}_d = \boldsymbol{u}_O + \boldsymbol{A}\boldsymbol{u}_W + \boldsymbol{u}_S. \qquad \textbf{(Model C)} \qquad (7)$$

A comparative analysis of the three models will be conducted later in this study (see Section 5.1), eventually motivating the selection of Model A for the physical module.

Once the drift velocity obtained, the forecasted position is integrated using Runge Kutta 4 scheme with a timestep of $t = 1$h.

3.1.3   From a predicted trajectory to a probability of presence

Numerical models are inherently chaotic, resulting in an extreme sensitivity to initial conditions. In addition, meteorological and oceanographic data also have their own uncertainties, as do the GPS positions of the objects provided to the model.

Moreover, because our model only predicts the next position and is run multiple times on successive obtained positions to get the full trajectory, we have an exponential propagation of errors. The trajectories produced can therefore change significantly if one slightly changes the initial data or the parameters of the model.

To address this uncertainty, we considered ensemble modeling [10][52][53]. The latter can be obtained using Monte Carlo simulations to cover a broad spectrum of possible scenarios by randomly and slightly modifying the initial position, the ocean surface, wind or Stokes field, as well as the parameters α and θ of the physical module.

More precisely, we iterate the computation of the predicted trajectory n times. During each iteration and for each variable, we introduce a random noise term $\varepsilon \sim \mathcal{N}(0, \sigma)$, where σ denotes the uncertainty associated with the variable, as provided by the dataset source. For α and θ, we choose values that encompass the range found in the literature (see Table 3). The selected uncertainties are summarized in Table 2.

Variable	σ
Initial position	100 m
$\boldsymbol{u}_O$	0.1 m/s
$\boldsymbol{u}_W$	0.15 m/s
$\boldsymbol{u}_S$	0.15 m/s
α	0.02
θ	10°

Table 2: Uncertainties of the data and parameters.

Following the calculation of the n trajectories, we obtain n potential positions for each time t. We then employ Kernel Density Estimation (KDE) [54] to derive a probability distribution of presence. The entire process is illustrated in Figure 7.
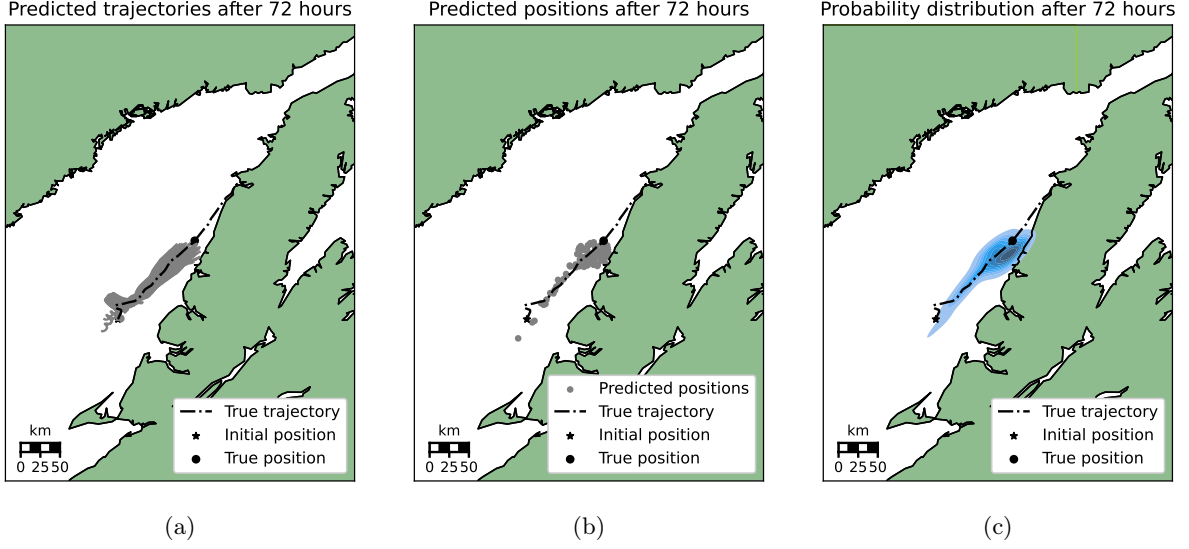
Figure 7: Illustration of the ensemble modeling method used to predict a map of the probability of presence of the floating object. (a) A set of n different trajectories is computed using slightly different initial conditions. (b) From the computed trajectories we extract the positions at the time of interest (here after 72 hours). (c) From those predicted positions we obtain a probability distribution using KDE.

3.2   Data-driven Model

To fully account for the spatial context surrounding the floating object as well as maintaining the 2-dimensional structure of the environmental data and consider the locality and the translation invariance inherent with those data, we decided to consider convolutional networks for the data-driven module, drawing inspiration from standard Convolutional Neural Networks (CNN). The architecture chosen, as well as the required data pre-processing and the further improvements proposed are described in the following subsections.

3.2.1   Data Processing and Context

Before being fed to the data-driven part of the model, the initial data undergo preprocessing to construct the contextual information, or context, surrounding the object This contextual information is represented as a tensor of dimensions $N \times N \times 6$. Each of the 6 channels represents a physical variable we want the model to account for, respectively the eastward- and northward- surface current velocities, the eastward- and northward- wind velocities and the eastward- and northward- Stokes drift. Attempts were made to incorporate bathymetry and the presence of coastlines as binary variables, but their inclusion did not lead to performance improvement. This outcome may be attributed to to the fact that the bathymetry takes on values that can vary by several orders of magnitude depending on the position of the object, and the frequent absence of coastlines over the entire considered area.

Each channel of the context is a $N \times N$ matrix with interpolated values of the physical variable

19

considered around the initial position. The context spans an area of $d \times d$ km. Typical values are $N = 32$ and $d = 50$km, as shown in Figure 8. These values are subject to change, but the distance d covered by the context must be large enough to allow for variations within that context. Because of the coarse resolution of the data (see Figure 8(b)) and because we interpolate the data to get the context, having an exceedingly large number of points N in the context does not further improve the performances.

(a)   (b)
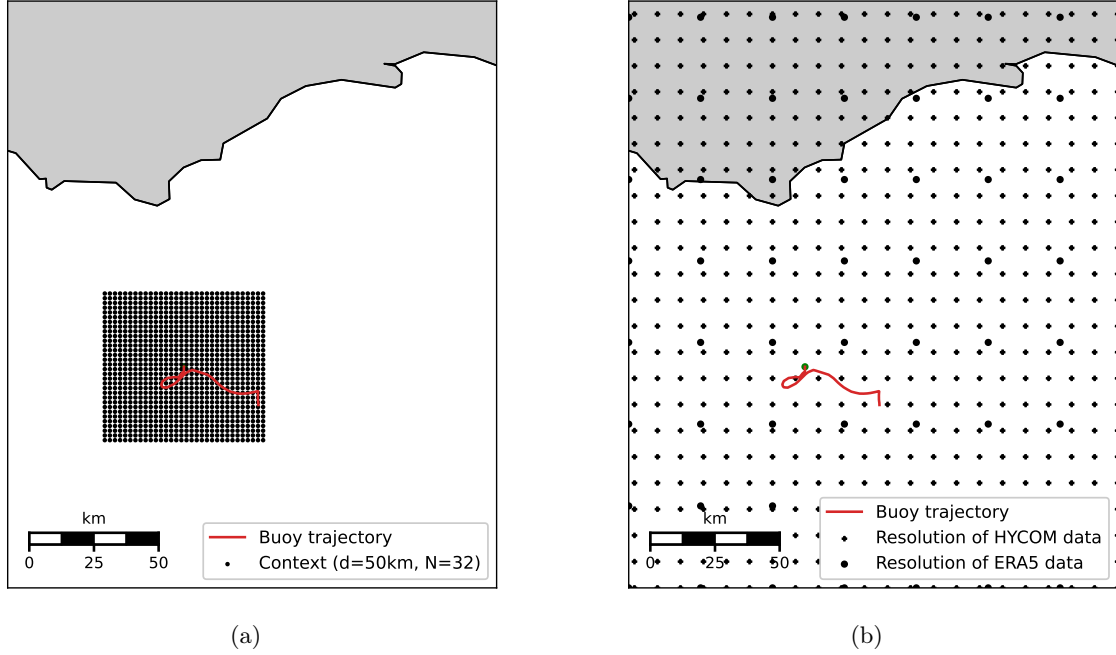
Figure 8: (a) Visualization of the area and resolution spanned by the context around the initial position of the buoy and (b) resolution of the initial data.

3.2.2   Architecture

The architecture of the data-driven module, presented in Figure 9 for a context with $N = 32$ points, is composed of a few convolutional layers with ReLU and Max-Pooling to encode the context, followed by a MLP with three hidden layers. The vector obtained is concatenated with the position predicted by the physical model, x_{phys}, before going through a final MLP with three hidden layers which outputs a correction to the physical prediction. The number of channels M_1 and M_2 as well as the size of the hidden layers are finetuned.

3.2.3   Incorporating Historical Positional Data

With the goal of enhancing the contextual understanding of our model and in the case where we know multiple successive positions of the floating object, it is possible to use not only one single initial position but several. We worked here with two known successive positions, separated by one
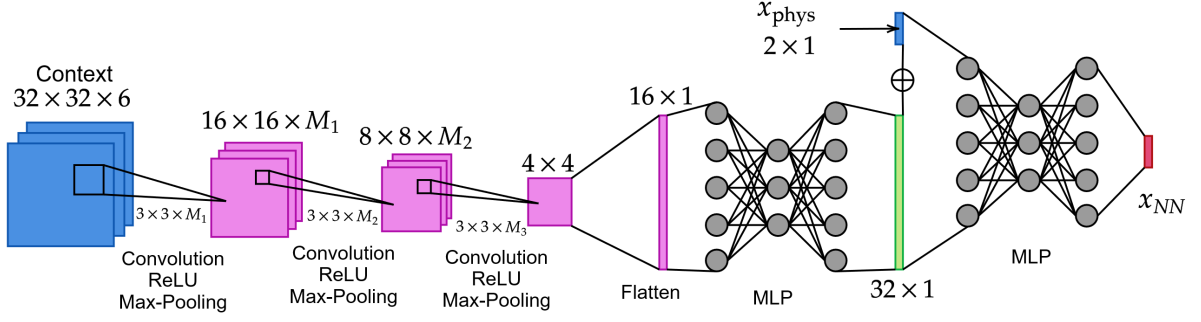
Figure 9: Data-driven module, for a context of size $N = 32$. For $N = 64$, also tested in this work, the architecture is similar except for the flattened vector obtained after the convolutions having a size of 64×1 instead of 16×1.

hour. In that case, the data-driven module is modified to account for the additional information. The contexts at t_0 and $t_0 - 1$h are concatenated to obtain a $N \times N \times 12$ tensor, and the position at $t_0 - 1$h is concatenated to the feature vector at the same time as the position obtained from the physical model, x_{phys}. The architecture of the module remains otherwise the same.

4 Experimental Setup

4.1 Preparation of the data

Datasets of drifters trajectories We have at our disposal two datasets of trajectories (see Section 2.1). Due to the limited amount of trajectories in the dataset of GPS drifters in Canada (Dataset 1) and due to the fact that it is geographically restricted to the St Lawrence estuary area, the latter is only used for the development and test of the physical module and does not require any further preparation.

On the contrary, the second dataset, more global and much larger requires some preprocessing. Out of the 17324 trajectories in the dataset, we randomly select 1000 of them to train the model. As trajectories can last up to a few months, and because we have an interest in predicting the position of the floating objects up to a few days after their detection only, the trajectories are limited to 72 hours. The selected dataset is split at a 70-20-10 ratio for training, validation and test set. The training dataset is provided in Figure 10. The validation and test dataset have similar distributions and are provided in Appendix B.
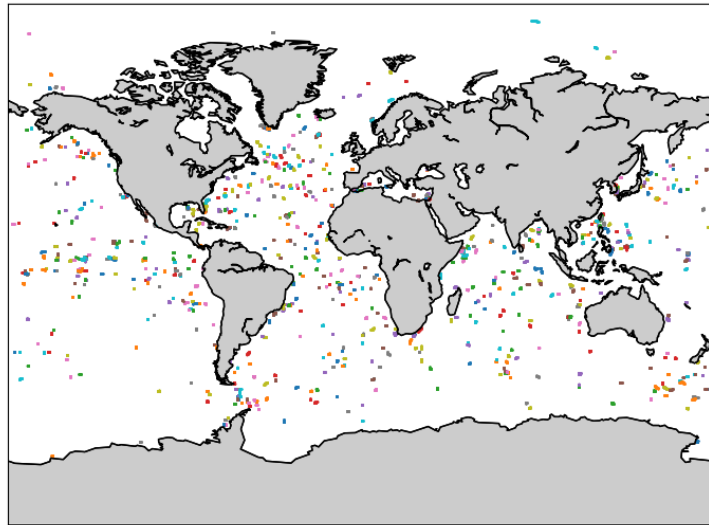
Figure 10: Training dataset of drifters trajectories.

Surface current, Wind and Stokes fields The vector fields did not require any particular pre-processing prior to training, apart from interpolation using the `RegularGridInterpolator` function from the `Scipy` library. Note that all the contexts of the training points are pre-computed prior to training, thereby mitigating the need for their recomputation during each epoch.

4.2   Training parameters

The model is trained on a single GPU with a batch size of 32. The optimal learning rate was found to be $1e^{-4}$ and the addition of learning rate decay did not prove helpful. The model is trained for a minimum of 150 epochs, and the trainer is then stopped after 20 validation checks with no improvement. Validation steps are run every epoch. The optimizer used is Adam. SGD was also tested but yielded poor results when compared with Adam.

4.3   Loss function and training strategy

The choice of the loss function, which compares the training data trajectory and the predicted solution plays a crucial role in the training of the model. It must be chosen in accordance with the goal of the optimized model, which in our case is dual: while we initially designed the model with the specific task of predicting the next position of the object only, thus emphasizing accuracy in this prediction, the overarching aim of the model is to forecast complete trajectories. This broader objective necessitates the model to possess an understanding of both time continuity and the concept of a trajectory. This duality must be reflected in the choice of the loss function and in the training strategy.

Haversine Loss   For the majority of the models trained, we choose to use the actual distance between the true and predicted positions at time t as the loss function. Because we are working with the geographic coordinate system and since the distances considered might be large enough for the curvature of the Earth to have an impact, the standard euclidean distance must be replaced by the haversine distance, defined as [55]:

$$\text{haversine}(\boldsymbol{x}, \boldsymbol{y}) = 2r \arcsin\left(\sqrt{\sin^2\left(\frac{\varphi_y - \varphi_x}{2}\right) + \cos(\varphi_x)\cos(\varphi_y)\sin^2\left(\frac{\lambda_y - \lambda_x}{2}\right)}\right), \quad (8)$$

with φ_x and φ_y the latitudes of true and predicted positions $\boldsymbol{x}$ and $\boldsymbol{y}$ and λ_x and λ_y their longitudes. Unless explicitly specified otherwise, this is the loss that is used in this work.

Angle Difference Loss   Although the haversine loss optimizes the length of the trajectory, it misses an essential aspect which is the angle of state space vectors. One way to counteract this weakness is to add a second component, namely the normalized difference between the angles between the two position vectors, i.e. a normalized cosine similarity to obtain the Length Difference and Angle Difference Loss [56]:

$$\text{LDA}(\boldsymbol{x}, \boldsymbol{y}) = \text{haversine}(\boldsymbol{x}, \boldsymbol{y}) + \frac{1}{2}\left(1 - \frac{(\boldsymbol{x} - \boldsymbol{x}_0) \cdot (\boldsymbol{y} - \boldsymbol{x}_0)}{\text{haversine}(\boldsymbol{x}, \boldsymbol{x_0}) \cdot \text{haversine}(\boldsymbol{y}, \boldsymbol{x_0})}\right). \quad (9)$$

The point $\boldsymbol{x}_0$ serves as an origin and is chosen as the initial position of the object.

Trajectory-based Loss Instead of confining the loss computation and training step exclusively to the prediction of the next position, an approach to improve the model's ability to forecast the entire trajectory and predict a global trend without altering its overall structure is to compute multiple successive positions before initiating a step. The loss must then reflect this change and the additional positions involved. One possibility is to use the normalized cumulative Lagrangian separation distance given by [30][35][32]:

$$sc(t_N) = \frac{\sum_{n=0}^{N} ds_n}{\sum_{n=0}^{N} L_n} = \frac{\sum_{n=0}^{N} ds_n}{\sum_{n=0}^{N} \sum_{m=0}^{n} dl_m}, \tag{10}$$

where L_n is the length of the observed trajectory at time t_n, $n = 0, ..., N$ corresponding to the observation points along the trajectory. ds_n represents the separation distance between observed and predicted position and dl_m corresponds to the distance between two consecutive observed positions (see Figure 11), both computed using the haversine distance. We used here $N = 3$ for training, i.e. we computed a 3-hour trajectory before updating the model.
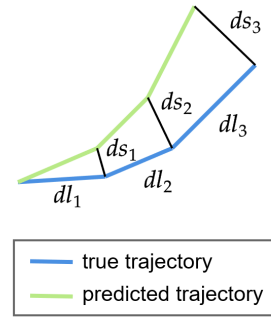
Figure 11: Illustration of the separation distances between predicted and observed trajectories used to compute the normalized cumulative Lagrangian separation distance.

This training strategy involves a dynamic computation of context during the training process. Contrary to the previous scenario where all positions employed during the model's training were predetermined, this strategy involves inherent uncertainty as the positions at $t + 1$ and $t + 2$, which evolve during the training process, serve also as inputs to the model. Given the computational expense associated with a dynamic computation of the context, we decided in this work to keep them consistent across an entire training step, specifically the context of the initial position is used for all subsequent position computations between two steps. This decision is grounded in the intuition that the environmental variables exhibit minimal change over the one-hour interval between two successive positions. It also finds justification in the observed very high correlation between the contexts at t and $t + 1h$, as observed in Figure 12.

4.4   Evaluation Metrics

The performances of a forecasting model are measured by its ability to generate:

- A predicted trajectory closely aligned, both spatially and temporally, with the actual trajectory.
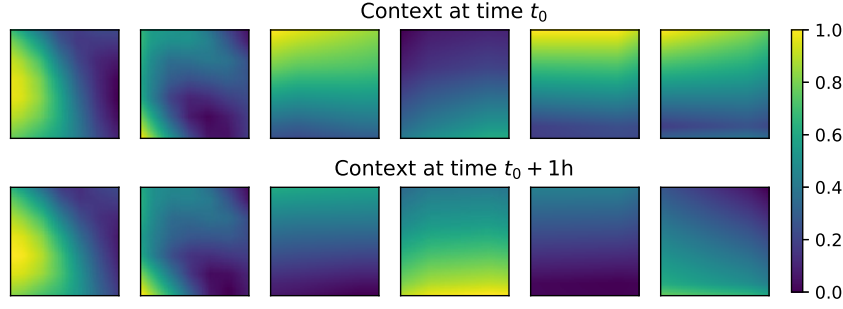
Figure 12: Visualization of the (normalized) context surrounding an object at two timesteps separated by one hour. Each column corresponds to a channel of the context. The Pearson correlation coefficient between the two flattened contexts is 0.99.

- A predicted probability of presence as described in section 3.1.3, centered around the true position and with minimal spatial extension. It is pertinent to note that the inherently chaotic nature of numerical predictions may lead to a gradual increase in spatial extension over time.

The metrics used are therefore separated into two distinct families: metrics for assessing the quality of individual trajectories; and metrics for measuring the quality of probability distributions of the floating object's position. These metrics range from fundamental measures of correlation and similarity to more specialized metrics particularly designed for drift trajectory estimation.

4.4.1   Metrics for trajectory evaluation

Separation distance   As with the training loss mentioned earlier, the most intuitive metric for assessing the performance of the drift models and their capacity to predict individual trajectories is the separation distance between observed and simulated drift trajectories, defined as:

$$ds(t) = \text{haversine}(\boldsymbol{x}_{\text{obs}}(t), \boldsymbol{x}_{\text{pred}}(t)). \tag{11}$$

The haversine distance is employed, as previously mentioned, to consider the Earth's geometry and the substantial scales involved.

The separation distance, extensively used in the literature [30][31][57], does, however, have some notable shortcomings and weaknesses. As demonstrated in [58], the latter is unable to demonstrate relative model performance in the presence of weak and strong currents. Moreover, its lack of normalization does not enable a proper comparison between predicted trajectories of different lengths (whether it be spatially or temporally).

Skill score and normalized cumulative Lagrangian separation distance   To address the limits of the separation distance, Li et al. [58] introduced the skill score, which is based on cumulative Lagrangian separation distances normalized by related cumulative trajectory lengths. More

precisely, and adopting the notations used by Tamtare et al.[30], the skill score is defined as:

$$ssc = \begin{cases} 1 - sc & \text{if} \quad sc \leq 1 \\ 0 & \text{if} \quad sc > 1, \end{cases} \tag{12}$$

where sc is the normalised cumulative Lagrangian separation distance defined in equation (10). The skill score takes values between 0 and 1, a skill score of 1 indicating a complete agreement between simulations and observations all along the trajectory. This metric is nowadays widely used, whether it be for oil spills models [35] or floating marine objects [30][32][31][59][60].

Time-averaged separation distance   Although not as often referred to as the skill score, the time-averaged distance *tad* as defined in [61] can also be used as a measure of the dissimilarity between two trajectories. In particular, the latter, which is essentially an average of the separation distance over time, addresses one of the key issues of the separation distance by allowing a proper comparison between two trajectories of different temporal lengths. It is defined as:

$$tad = \frac{1}{t_N - t_0} \sum_{n=0}^{N} \text{haversine}(\boldsymbol{x}_{\text{obs}}(t_n), \boldsymbol{x}_{\text{pred}}(t_n)) = \frac{1}{t_N - t_0} \sum_{n=0}^{N} ds(t_n).$$

Correlation coefficient   Eventually, an important category of similarity measures that we have not considered yet is the correlation coefficients. Widely used in statistics, where a high correlation between trajectories will mean a high similarity, correlation coefficients have also been previously used for drift models assessment [30][31]. However, once again, there are a few limitations to be aware of.

Firstly, although the correlation coefficient is perfectly defined for one-dimensional variables (via Pearson's correlation coefficient, for example), in the case of multidimensional variables is more complex. Multiple definitions exist, such as the Canonical Correlation Coefficient (CAC), the RV Coefficient, Distance Correlation (dCor), or the Generalized Multiple Correlation Coefficient defined by Urain et al. [62]. While earlier investigations utilizing correlation coefficients for drift trajectories resorted to employing complex velocities to simplify the analysis back to the one-dimensional scenario and mitigate confusion, handling multidimensional variables, including velocities or positions, inherently complicates the application of correlation coefficients.

Secondly, and this applies to both unidimensional coefficients and their multidimensional versions, the correlation coefficients remain invariant to linear transformations, and sometimes orthogonal transformations and rotations (RV coefficient) or even non-linear transformations (dCor). While these properties are desirable in various domains, such as in robotics for learning human movements [62], they pose challenges in the context of drift trajectory estimation. Specifically, a metric invariant to rotation, for instance, fails to distinguish between a trajectory heading north and its spherical symmetry heading south. Similarly, a metric invariant to linear transformations perceives a trajectory and its 'slowed down' version as similar. In both scenarios, humans would typically consider

the prediction of a rotated or scaled trajectory as unacceptable, whereas correlation coefficients would indicate a high similarity with the observed trajectory.

This is the main reason why correlation coefficients will not be used in this work. For the interested reader, a more in-depth study of these correlation coefficients as well as many tests on trajectories were carried out by Urain et al. [62].

4.4.2 Metrics for probability density assessment

If measuring the similarity between a predicted trajectory and a true trajectory is quite intuitive, assessing the quality of a probability distribution given the true observed position is a bit more difficult.

Mean and standard deviation   We want the predicted probability distribution to be:

- centered around the true observed position, that is we want the distance between the centroïd of the distribution and the true position to be small,

- peaked around the true observed position, that is we want the point with the highest probability of presence to be close to the true position,

- as little spread as possible, i.e. we want its standard deviation to be small.

Therefore, very intuitive metrics are:

1. The distance between the centroïd $\boldsymbol{\mu}$ of the predicted probability density function and the observed position $\boldsymbol{x}_{\mathrm{obs}}$:
$$d_\mu = \mathrm{haversine}(\boldsymbol{\mu}, \boldsymbol{x}_{\mathrm{obs}}) \tag{13}$$

2. The distance between the mode $\boldsymbol{\nu}$, i.e. the point of the predicted probability density function with the highest probability and the observed position $\boldsymbol{x}_{\mathrm{obs}}$:
$$d_\nu = \mathrm{haversine}(\boldsymbol{\nu}, \boldsymbol{x}_{\mathrm{obs}}) \tag{14}$$

3. The standard deviation σ of the predicted probability density function.

These three metrics can be obtained for each time step. In particular, the sequence of successive centroids, as well as the sequence of successive modes both create a possible trajectory of the floating object. These trajectories can then undergo evaluation using the metrics introduced earlier in Section 4.4.1, providing alternative methods for assessing model performance. In particular, we will compute the skill scores of the centroïds and nodes trajectories, noted ssc_μ and ssc_ν respectively. Note that the trajectories of the centroïds (and nodes respectively) can also be used as predicted trajectories of the model, with the advantage of them being less sensitive to noise and perturbations.

27

Averaged Negative Log-Likelihood A second method to assess the quality of the probability distribution obtained from the Kernel Density Estimation is to compute the negative log-likelihood of the ground truth trajectory, noted *nll*. The negative log-likelihood is computed for each time step, and can eventually be averaged over time to enable comparison of trajectories with different durations. We obtain the averaged negative log-likelihood:

$$anll = \frac{1}{t_N - t_0} \sum_{n=0}^{N} nll = \frac{1}{t_N - t_0} \sum_{n=0}^{N} -\log(p(\boldsymbol{x}_{\text{obs}}|f_{\text{KDE}})), \tag{15}$$

where f_{KDE} is the probability density function obtained from the Kernel Density Estimation.

4.5   Fine-tuning of the model and optimal parameters

4.5.1   Fine-tuning of the physical module

The physical models presented in Section 3.1 predominantly depend on oceanographic and meteo-rological data; however, for models A and C, it is imperative to furnish the values of the drift factor α and the drift angle θ. In consideration of the fundamental physical principles underlying these models (see equation (1)), it is anticipated that α will approximate the Nansen number, and θ is expected to fall within the range of 20° to 40° in the northern hemisphere. Because this angle is intimately linked to the Coriolis force, it is however expected to vary significantly with the latitude. Previous experimental surveys reported values between 0.01 and 0.06 for α and 10° and 50° for θ. The values reported in various studies are compiled in Table 3.

Authors	$\alpha(\%)$	θ	Remarks
Smith (1968) [63]	3.3	10.4°	Oil spills from the Torrey Canyon
Al Rabeh (1994) [27]	3.1	27.42°	Oil spills in the Arabian Gulf
Spaulding et al. (1993) [64]	3	3°	Modelization of oil spills in the Arabian Gulf
De Aguiar et al. (2023) [10]	3	0°	Ensemble drift predictions of oil slicks
Smith and Banke (1983) [65]	2	$12° - 34°$	Drift of icebergs
Garrett et al. (1985) [66]	1.8	-	Drift of icebergs off the coast of Labrador
Daniele et al. (2002) [67]	0-10	-	Drift of containers
De Dominicis et al. (2013) [34]	0-3	$0° - 25°$	Surface drifters in the Mediterranean Sea
Tamtare et al. (2019-2021) [30][31]	1.1-2.3	$1° - 50°$	Drifting buoys in the Estuary and Gulf of St. Lawrence

Table 3: Reported values for the drift factor α and drift angle θ.

This table serves to point out the fact that there exist large discrepancies between the values found by different studies. To reflect this aspect, as well as the fact that these parameters may depend on the nature and shape of the object (e.g. how much it is exposed to the wind), we decided in this work to allow for these parameters to be empirically fine-tuned for each individual floating object.

The choice of optimal parameters can be formulated as the following optimization problem:

$$\min_{\alpha,\theta} \frac{1}{2}\|\boldsymbol{u}_{d,true} - \boldsymbol{u}_{d,pred}\|_2^2 = \boldsymbol{f}, \tag{16}$$

with $\boldsymbol{u}_{d,true}$ obtained from two consecutive known positions using finite differences and $\boldsymbol{u}_{d,pred}$ provided by models A or C. The parameters are then updated using gradient descent:

$$\begin{pmatrix} \alpha_{\text{new}} \\ \theta_{\text{new}} \end{pmatrix} = \begin{pmatrix} \alpha \\ \theta \end{pmatrix} - \gamma\nabla_{\alpha,\theta}\boldsymbol{f}, \tag{17}$$

with γ the step size. Given the disparate orders of magnitude between α and θ, a prudent approach involves employing distinct steps for each parameter. Consequently, γ is established at 10% of the initial values of α and θ respectively. In accordance with the results gathered in Table 3, the initial values assigned to α and θ are set to

$$\alpha_{\text{init}} = 0.03 \qquad \text{and} \qquad \theta_{\text{init}} = 20°.$$

The repetition of the aforementioned update step is contingent upon the quantity of available known positions. As the number of known positions increases, the parameters become more specific to the object, ideally resulting in an enhanced model performance.

Note that because the angle θ is expected to be intrinsically linked to the latitude due to the Coriolis force, another approach could have been to parametrize its value based on the latitude. However, as shown in Figure 13, no correlation between the angle between the wind direction and the object direction and the latitude has been found for the trajectories of the drifting buoys of the Global Drifter Program (Dataset 2). This approach has therefore not been retained here.
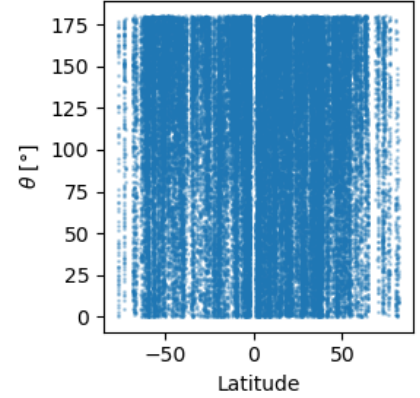
Figure 13: Measured value of θ, the angle between the wind direction and the object velocity, with respect to the latitude for the trajectories of the drifting buoys of the Global Drifter Program (Dataset 2).

4.5.2   Fine-tuning of the data-driven module

For the data-driven module, the optimal training parameters have been obtained using the `optuna` framework [68]. 100 tests with various parameters combinations have been made, yielding the optimal parameters gathered in Table 4. Note that the choice of the optimal parameters has been done on the hybrid model trained with a context of $d = 50$km with $N = 32$ points, the standard haversine loss, and without the use of previous positions. These optimal parameters have then been used for the other configurations of the model.

Parameter	Range of values tested	Optimal value
M_1	[16,64]	32
M_2	[16,64]	19
M_3	-	1
hidden$_1$	[64,256]	225
hidden$_2$	[64,256]	73
hidden$_3$	-	32
hidden$_4$	[64,256]	188
hidden$_5$	[64,256]	66
hidden$_6$	-	2

Table 4: Optimal values for the parameters of the data-driven module (Figure 9 and section 3.2). $M_{1,2,3}$ correspond to the numbers of channels of the convolution kernels, hidden$_{1,2,3}$ to the sizes of the hidden layers of the first MLP and hidden$_{4,5,6}$ to the sizes of the hidden layers of the second MLP. M_3, hidden$_3$ and hidden$_6$ are fixed.

5   Results

This section presents the results of the evaluation of the model presented in Section 3. This evaluation is carried out in two phases. The physical module is first evaluated alone. Evaluation is made on Dataset 1 (Canada data). The primary objective of this initial phase is to assess the added value brought by the inclusion of Stokes drift in the model. Specifically, a comparison is made among Models A, B, and C as described in Section 3.1. Both the trajectories predicted and the probability distributions of presence obtained are evaluated.

In a second time, the data-driven part is added and the entire model is this time tested on Dataset 2, its large size and diversity allowing for better and more global training of the data-driven module. The optimal model identified in the assessment of the physical module is utilized within this component of the overall model.

The aim of this second experiment is multiple:

1. Determine the optimal number of points N and area spanned d of the context, as described in section 3.2.1. Through empirical observation, it was determined that contexts encompassing a restricted area (within the range of 1 km to 10 km) were insufficient to capture the variations in environmental data. As a pragmatic choice, we decided to investigate contexts of sizes $N = 32$ and $N = 64$, covering areas of $d = 50$ km and $d = 100$ km, respectively.

2. Determine the optimal loss and training strategy among the three described in section 4.3.

3. Assess the impact of incorporating historical data, as explained in Section 3.2.3, on the predictive performance.

Six models are formulated to address the three stated objectives, covering various scenarios:

- **Model K**: This serves as the baseline hybrid model, employing a context of size $N = 32$ spanning an area of $d = 50$ km. It is trained using the haversine loss without angle correction and without incorporating additional historical data.

- **Model L and M**: These two models investigate the influence of the number of points N and area spanned d of the context. Model L features a context of size $N = 32$ and $d = 100$ km, while Model M adopts a context of size $N = 64$ and $d = 50$ km. Both are trained using the haversine loss without angle correction and additional historical data.

- **Model N**: This model is similar to Model K but utilizes the angle difference loss in place of the haversine loss.

- **Model O**: This model incorporates the use of the previous position as described in section 3.2.3. It uses a context of size $N = 32$ spanning an area of $d = 50$ km and is trained with the haversine loss.

- **Model P**: This final model uses the trajectory-based loss. It does not use additional historical data and has a context of size $N = 32$ spanning an area of $d = 50$km.

5.1 Evaluation of the physical model

This section presents the outcomes of the evaluation conducted on Dataset 1 for the physical model. The principal aim of this preliminary investigation is to evaluate the enhanced performance resulting from the incorporation of Stokes drift in the model, as outlined in Models A, B, and C in Section 3.1. The models are initially qualitatively compared by examining predicted trajectories and probability maps of presence on a few selected examples. Then, this qualitative analysis is extended to encompass all traces in the dataset, enabling the derivation of more quantitative measures for comparison. The contribution of each forcing term (Ocean surface current, wind velocity, Stokes field) is also assessed.

5.1.1 Qualitative results and comparison

Three examples of predicted and observed drifting trajectories are presented in Figure 14 at different locations in the Estuary and Gulf of St. Lawrence and at different times. Despite some discrepancies, the three models provide rather good predictions and are able to fully outline the global trend of the trajectory. In addition, none of the three models really outperforms the two others, and it is difficult at this point to conclude whether or not Stokes drift should be considered.
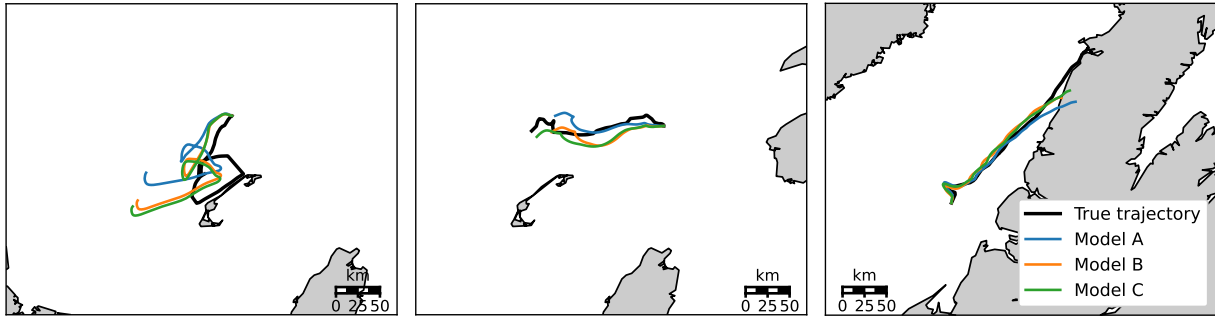
Figure 14: Examples of three observed drifters trajectories (black) and trajectories simulated by model A (blue), model B (orange) and model C (green).

Turning to the probability of presence, an example of the temporal evolution of the predicted probability is shown in Figure 15. We observe the expected behavior where the spread of the probability density increases substantially with time. This expansion is a consequence of the inherent propagation of errors during the computation of the trajectory.

Eventually, it is worth noting that the mode $\boldsymbol{\nu}$ of the predicted probability density function; i.e.

the point with the highest probability lies in close proximity to the true observed position of the drifting buoy. This observation confirms the ensemble method's efficacy in mitigating the effects of uncertainties stemming from the model, environmental factors, and positional data.
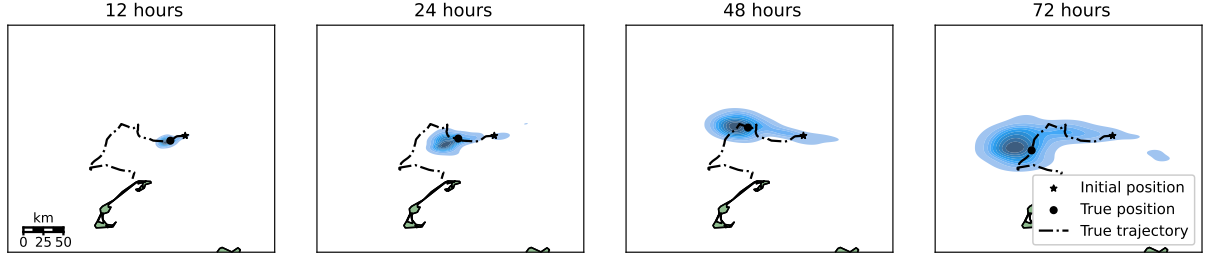
Figure 15: Example of estimated probability of position of the floating object after 12, 24, 48 and 72 hours.

5.1.2   Contribution of each forcing term

In the investigation of drift velocity prediction, the analysis of each forcing term's contribution is crucial. Such an exploration is essential for a comprehensive understanding of the underlying dynamics governing drift velocity prediction and contributes to the refinement of predictive models. Figure 16 illustrates the time series of relevant velocities for two 72-hour trajectories extracted from Dataset 2. This figure enables the examination and discernment of the individual contributions of various environmental variables to the predicted drift velocity.

First, it is worth noticing that the leading components influencing drift velocity can change. Specifically, it is observed that in certain instances, the preeminent factor influencing the drift velocity is the ocean surface current, a phenomenon consistently observed for the first trajectory. Additionally, the wind emerges as a significant contributor to drift velocity, particularly evident in the second trajectory between the 15th and 25th hours and again after the 55th hour. This temporal variability underscores the complexity of the interactions between environmental variables and their impact on trajectory predictions. Furthermore, the figure reveals that the Stokes drift exerts a relatively minor influence on the overall drift velocity, and it appears to exhibit a strong correlation with wind velocity.

This strong correlation between the wind velocity and Stokes drift, intuitively understood by the fact that waves are mostly driven by the wind, is further explored in Figure 17. It outlines the similarities between the variations of the eastward and northward wind velocities and the Stokes field. With a Pearson correlation coefficient of 0.90 encompassing a strong and non-negligible correlation between the two variables, it can be argued that it is not necessary to keep both variables in the drift model. More precisely, it can be supported that the effect of the waves and Stokes drift are accounted for in the drifting factor α and drifting angle θ preceding the wind velocity term. This analysis thus suggests preferring models A and B to model C, but does not enable a proper conclusion on the
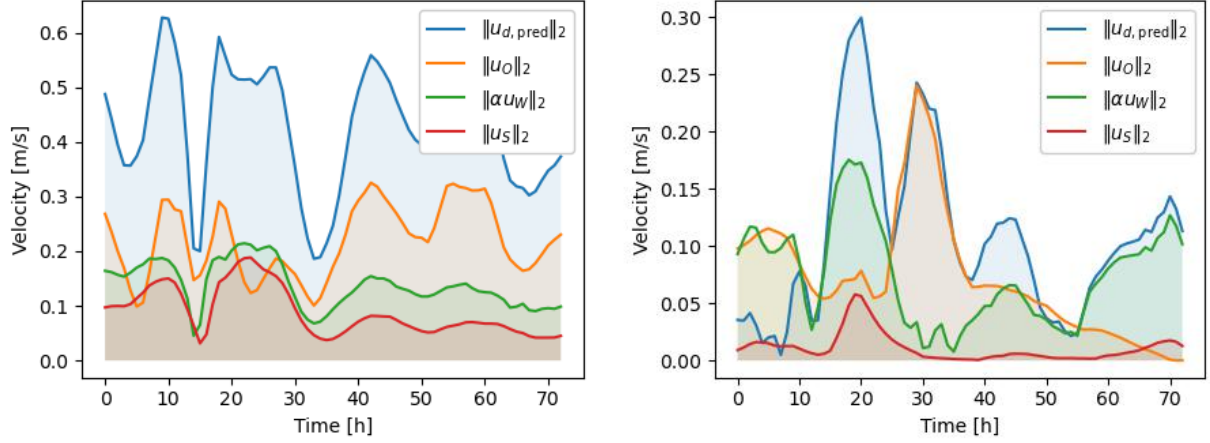
Figure 16: Time series of relevant velocities for two 72-hour trajectories from Dataset 2. The drift velocity $\|u_{d,\text{pred}}\|_2$ is obtained using model C. This Figure allows the observation of the contribution of each environmental variable in the predicted drift velocity.

necessity of including the Stokes drift in the prediction.
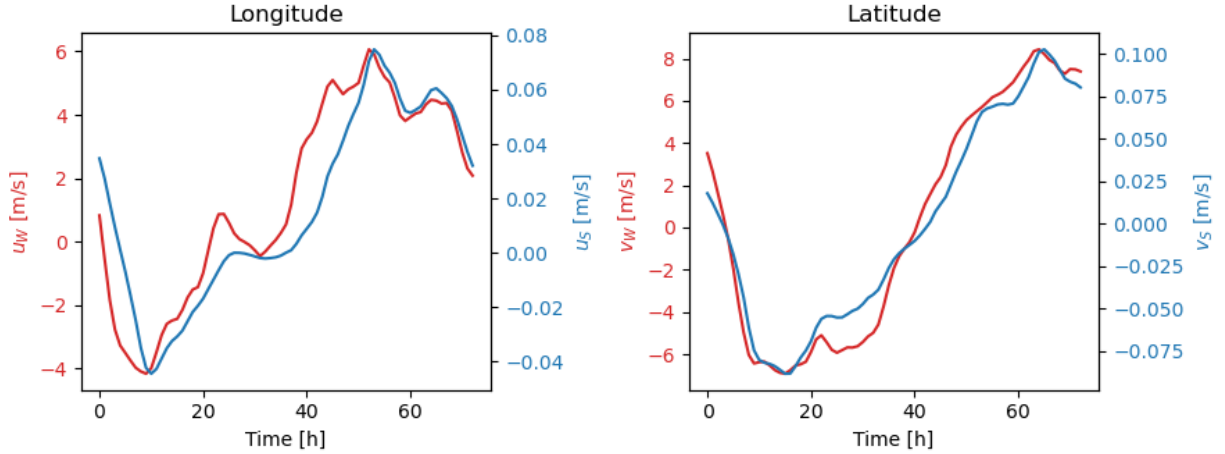
Figure 17: Comparison of the longitudinal and latitudinal wind velocity and Stokes drift for a random trajectory in Dataset 2. The Pearson correlation coefficient between the wind velocity and Stokes drift is 0.90 (pvalue = 4e-27). This example is representative of the whole dataset.

5.1.3   Quantitative comparison

Based on the few instances observed in Section 5.1.1 and 5.1.2 only, it is difficult to determine which of these models performs better in all cases and if the addition of the Stokes field in the drift velocity has a clear positive impact on the prediction. As a result, an objective assessment of the capabilities of the various drift models on the 103 trajectories of Dataset 1 is performed below using the metrics described in Section 4.4.

The results are aggregated in Table 5 for different forecast periods ranging from 3h to 72h. As anticipated, the inevitable propagation of errors leads to an increase of the separation distance d_s and time-averaged distance tad with time. More surprisingly, we have an increase in the skill score ssc with time, indicating an increase in the agreement between simulated and observed trajectories. Although this seems contradictory to the previous remarks on separation distance and time-averaged distance, it is actually the result of the normalization performed. For very short trajectories, despite the small separation distance, the normalized Lagrangian distance is very large, resulting in a very low skill score. On the contrary, the prediction error is far more mitigated by trajectory length when the prediction time is greater. Therefore, looking at the bigger picture, the overall quality of trajectories improves with time. The model exhibits challenges in predicting the initial stages of the trajectory but demonstrates improved accuracy in capturing the overall trend. Similar observations have been previously documented by Tamtare et al. [30].

Similar observations apply to the probabilities of presence. The negative log-likelihood, along with the distances d_μ and d_ν between the true position and the centroid or mode of the distribution increase with time. This trend indicates that the density obtained becomes less accurate with the elapsed time. Its uncertainty is also increasing, as indicated by the rise in its deviation σ. For skills scores associated with the centroid and mode, the same remarks can be made as above.

Upon comparing the three models, which is the primary objective of this first experiment, the results are somewhat underwhelming. The observed differences are minimal and lack statistical significance. It appears that the intuition expressed in the preceding section has been validated: wind speed and the Stokes field may be redundant for the model. Not only is there no apparent need to consider both simultaneously for prediction, but it is challenging to determine which of the two elements yields superior predictions. For pragmatic reasons, such as the higher resolution of wind data and the minor differences observed, we opt for Model A as the physical module for the remainder of this study, both as a standalone physics model and as part of the hybrid model.

5.1.4 Limitations of the physical model

Despite their apparent effectiveness in accurately predicting buoy trajectories, the three physical models mentioned above present some notable difficulties. As mentioned earlier, they encounter difficulties in predicting the beginning of the trajectories. Additionally, there is a notable struggle in predicting tracks close to the coast, as illustrated in Figure 18.

The experiment summarized in Table 5 was reiterated in Table 6, focusing exclusively on trajectories situated far away from the coast. The metrics demonstrate enhanced performance, suggesting once again that one of the principal difficulties of the model resides in predicting trajectories near the coast.

Table 5: Averaged drift model performances (103 trajectories). Bold values represent the best performances. Uncertainties represent standard deviations for 10000 bootstrap resamples.

Metric	Time	Model A $u_d = u_O + Au_W$	Model B $u_d = u_O + u_S$	Model C $u_d = u_O + Au_W + u_S$
d_s [km]				
	3h	**3 ± 1**	4 ± 1	4 ± 1
	6h	**6 ± 1**	7 ± 1	7 ± 1
	12h	**11 ± 2**	**11 ± 2**	12 ± 2
	24h	18 ± 3	18 ± 2	18 ± 3
	48h	**27 ± 4**	**27 ± 4**	28 ± 4
	72h	**32 ± 6**	33 ± 6	35 ± 6
ssc				
	3h	**0.30 ± 0.06**	0.22 ± 0.05	0.26 ± 0.06
	6h	**0.32 ± 0.06**	0.26 ± 0.05	0.29 ± 0.05
	12h	**0.36 ± 0.05**	0.32 ± 0.05	0.33 ± 0.05
	24h	**0.42 ± 0.06**	0.40 ± 0.05	0.40 ± 0.05
	48h	0.42 ± 0.06	**0.44 ± 0.05**	0.42 ± 0.05
	72h	0.48 ± 0.06	**0.50 ± 0.05**	0.47 ± 0.05
tad [km/h]				
	3h	**2.5 ± 0.9**	2.6 ± 0.9	**2.5 ± 0.9**
	6h	4 ± 1	4 ± 1	4 ± 1
	12h	7 ± 1	7 ± 1	7 ± 1
	24h	10 ± 2	10 ± 1	10 ± 1
	48h	17 ± 2	**16 ± 2**	17 ± 2
	72h	22 ± 3	**21 ± 3**	22 ± 3
nll				
	3h	1.839 ± 0.001	1.839 ± 0.001	1.839 ± 0.001
	6h	1.841 ± 0.001	1.841 ± 0.001	1.841 ± 0.001
	12h	1.846 ± 0.002	**1.844 ± 0.002**	1.846 ± 0.002
	24h	1.858 ± 0.005	**1.854 ± 0.002**	1.858 ± 0.004
	48h	1.877 ± 0.008	**1.87 ± 0.01**	1.88 ± 0.01
	72h	**1.89 ± 0.01**	**1.89 ± 0.02**	1.90 ± 0.02
$anll$	/	1.866 ± 0.006	**1.862 ± 0.007**	1.868 ± 0.007
d_μ [km]				
	3h	4 ± 1	4 ± 1	4 ± 1
	6h	7 ± 1	7 ± 1	7 ± 1
	12h	12 ± 2	**11 ± 2**	**11 ± 2**
	24h	20 ± 2	**18 ± 2**	**18 ± 3**
	48h	30 ± 3	**27 ± 4**	29 ± 4
	72h	37 ± 5	**33 ± 6**	38 ± 6
d_ν [km]				
	3h	4 ± 1	4 ± 1	4 ± 1
	6h	**6 ± 1**	7 ± 1	7 ± 1
	12h	**11 ± 2**	**11 ± 2**	12 ± 2
	24h	**17 ± 3**	18 ± 2	19 ± 3
	48h	**26 ± 4**	27 ± 4	30 ± 4
	72h	**31 ± 5**	33 ± 6	35 ± 6
σ [km]				
	3h	1.8 ± 0.2	**0.50 ± 0.05**	1.4 ± 0.2
	6h	3.5 ± 0.5	**0.65 ± 0.07**	2.7 ± 0.5
	12h	7 ± 1	**0.9 ± 0.1**	5 ± 1
	24h	12 ± 2	**1.3 ± 0.2**	10 ± 2
	48h	19 ± 3	**1.9 ± 0.3**	15 ± 3
	72h	23 ± 4	**2.3 ± 0.4**	18 ± 4
ssc_μ				
	3h	**0.24 ± 0.04**	0.22 ± 0.05	**0.24 ± 0.05**
	6h	024 ± 0.05	0.26 ± 0.05	**0.27 ± 0.05**
	12h	0.30 ± 0.04	0.32 ± 0.05	**0.33 ± 0.05**
	24h	0.36 ± 0.05	0.40 ± 0.05	**0.41 ± 0.05**
	48h	0.38 ± 0.05	**0.44 ± 0.05**	0.43 ± 0.05
	72h	0.43 ± 0.05	**0.50 ± 0.05**	0.46 ± 0.05
ssc_ν				
	3h	**0.31 ± 0.06**	0.22 ± 0.05	0.22 ± 0.05
	6h	**0.33 ± 0.06**	0.26 ± 0.05	0.25 ± 0.05
	12h	**0.37 ± 0.06**	0.32 ± 0.05	0.27 ± 0.04
	24h	**0.44 ± 0.06**	0.40 ± 0.05	0.36 ± 0.05
	48h	**0.45 ± 0.06**	0.44 ± 0.05	0.39 ± 0.05
	72h	**0.50 ± 0.06**	**0.50 ± 0.05**	0.45 ± 0.05

36

Table 6: Averaged drift model performances for trajectories far from the shores and over 72 hours (37 trajectories). Bold values represent the best performances. Uncertainties represent standard deviations for 10000 bootstrap resamples.

Metric	Time	Model A $u_d = u_O + Au_W$	Model B $u_d = u_O + u_S$	Model C $u_d = u_O + Au_W + u_S$
d_s [km]				
	3h	$\mathbf{1.9 \pm 0.3}$	2.2 ± 0.3	2.0 ± 0.4
	6h	$\mathbf{3.5 \pm 0.6}$	4.1 ± 0.6	3.8 ± 0.7
	12h	6.5 ± 0.8	$\mathbf{5.7 \pm 0.8}$	7 ± 1
	24h	13 ± 2	$\mathbf{12 \pm 2}$	13 ± 2
	48h	$\mathbf{19 \pm 3}$	$\mathbf{19 \pm 3}$	21 ± 4
	72h	$\mathbf{23 \pm 4}$	$\mathbf{23 \pm 6}$	27 ± 6
ssc				
	3h	$\mathbf{0.44 \pm 0.09}$	0.37 ± 0.09	$\mathbf{0.44 \pm 0.09}$
	6h	$\mathbf{0.46 \pm 0.09}$	0.39 ± 0.09	0.45 ± 0.09
	12h	$\mathbf{0.48 \pm 0.08}$	0.47 ± 0.08	0.47 ± 0.07
	24h	0.52 ± 0.07	$\mathbf{0.53 \pm 0.06}$	0.52 ± 0.06
	48h	0.52 ± 0.07	$\mathbf{0.57 \pm 0.06}$	0.53 ± 0.06
	72h	0.59 ± 0.06	$\mathbf{0.61 \pm 0.06}$	0.58 ± 0.06
tad [km/h]				
	3h	$\mathbf{1.3 \pm 0.2}$	1.5 ± 0.2	$\mathbf{1.3 \pm 0.3}$
	6h	$\mathbf{2.1 \pm 0.3}$	2.5 ± 0.4	2.2 ± 0.4
	12h	$\mathbf{3.7 \pm 0.5}$	3.8 ± 0.5	3.9 ± 0.6
	24h	6.6 ± 0.9	$\mathbf{6.4 \pm 0.7}$	7 ± 1
	48h	12 ± 1	$\mathbf{11 \pm 1}$	12 ± 2
	72h	$\mathbf{15 \pm 2}$	$\mathbf{15 \pm 2}$	16 ± 2
nll				
	3h	1.8382 ± 0.0001	$\mathbf{1.8381 \pm 0.0001}$	1.8382 ± 0.0001
	6h	1.8390 ± 0.0004	$\mathbf{1.8387 \pm 0.0002}$	1.8393 ± 0.0006
	12h	1.841 ± 0.001	$\mathbf{1.8394 \pm 0.0004}$	1.842 ± 0.002
	24h	1.850 ± 0.005	$\mathbf{1.844 \pm 0.002}$	1.850 ± 0.004
	48h	1.862 ± 0.006	$\mathbf{1.855 \pm 0.005}$	1.869 ± 0.009
	72h	1.872 ± 0.005	$\mathbf{1.87 \pm 0.02}$	1.89 ± 0.02
$anll$	/			
d_μ [km]				
	3h	2.5 ± 0.5	$\mathbf{2.2 \pm 0.3}$	2.3 ± 0.3
	6h	4.8 ± 0.7	$\mathbf{4.1 \pm 0.6}$	4.3 ± 0.6
	12h	7 ± 1	$\mathbf{5.6 \pm 0.8}$	5.8 ± 0.7
	24h	15 ± 2	$\mathbf{12 \pm 2}$	$\mathbf{12 \pm 2}$
	48h	25 ± 3	$\mathbf{19 \pm 3}$	24 ± 4
	72h	31 ± 5	$\mathbf{23 \pm 6}$	32 ± 7
d_ν [km]				
	3h	$\mathbf{2.0 \pm 0.3}$	2.2 ± 0.3	2.5 ± 0.4
	6h	$\mathbf{3.6 \pm 0.8}$	4.1 ± 0.6	5.1 ± 0.8
	12h	7 ± 1	$\mathbf{5.7 \pm 0.8}$	9 ± 1
	24h	$\mathbf{12 \pm 2}$	$\mathbf{12 \pm 2}$	13 ± 2
	48h	$\mathbf{18 \pm 3}$	19 ± 3	24 ± 4
	72h	$\mathbf{22 \pm 4}$	23 ± 6	28 ± 5
σ [km]				
	3h	2.5 ± 0.4	$\mathbf{0.70 \pm 0.02}$	2.4 ± 0.3
	6h	4.9 ± 0.7	$\mathbf{0.97 \pm 0.02}$	4.7 ± 0.6
	12h	10 ± 1	$\mathbf{1.35 \pm 0.03}$	9 ± 1
	24h	17 ± 3	$\mathbf{1.96 \pm 0.05}$	16 ± 3
	48h	26 ± 4	$\mathbf{2.9 \pm 0.1}$	24 ± 4
	72h	34 ± 5	$\mathbf{3.6 \pm 0.1}$	30 ± 4
ssc_μ				
	3h	0.30 ± 0.08	0.36 ± 0.09	$\mathbf{0.37 \pm 0.09}$
	6h	0.31 ± 0.08	$\mathbf{0.39 \pm 0.09}$	$\mathbf{0.39 \pm 0.09}$
	12h	0.38 ± 0.07	$\mathbf{0.47 \pm 0.08}$	$\mathbf{0.47 \pm 0.08}$
	24h	0.43 ± 0.07	$\mathbf{0.53 \pm 0.05}$	0.52 ± 0.06
	48h	0.46 ± 0.06	$\mathbf{0.57 \pm 0.06}$	0.52 ± 0.06
	72h	0.51 ± 0.05	$\mathbf{0.62 \pm 0.06}$	0.55 ± 0.06
ssc_ν				
	3h	$\mathbf{0.44 \pm 0.09}$	0.36 ± 0.09	0.35 ± 0.09
	6h	$\mathbf{0.46 \pm 0.09}$	0.39 ± 0.09	0.36 ± 0.09
	12h	$\mathbf{0.48 \pm 0.09}$	0.47 ± 0.08	0.36 ± 0.07
	24h	0.52 ± 0.08	$\mathbf{0.53 \pm 0.05}$	0.44 ± 0.07
	48h	0.54 ± 0.08	$\mathbf{0.57 \pm 0.06}$	0.47 ± 0.07
	72h	0.61 ± 0.07	$\mathbf{0.62 \pm 0.06}$	0.53 ± 0.06

This challenge may stem from the complex physical dynamics prevalent in coastal regions, which cannot be adequately captured by the simplifications made in our models. These observed difficulties lead to the consideration of potential data-driven corrections and the subsequent experiments discussed in the following sections.
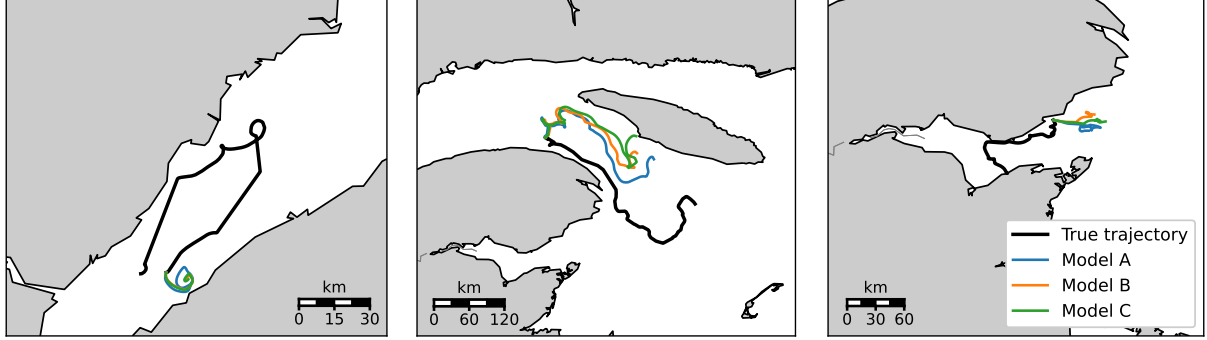

Figure 18: Examples of three observed drifters' trajectories (black), that model A (blue), model B (orange) and model C (green) fail at predicting.

5.2   Evaluation of the hybrid model

The second part of this work is dedicated to the evaluation of the hybrid model and its different enhancements. Analogous to the approach taken with the physical module, the models are initially explored qualitatively to develop an understanding of their potential successes and challenges. Figures 19 and 20 showcase examples of observed and predicted trajectories. Predictions are generated using the physical module alone (Model A) and with the baseline hybrid model (Model K). Discerning the true improvement brought by the data-driven correction is challenging at this point. In some cases (Figure 19), improved predictions were observed, both near and far from the coasts, while the opposite scenario was also frequently noted (Figure 20).
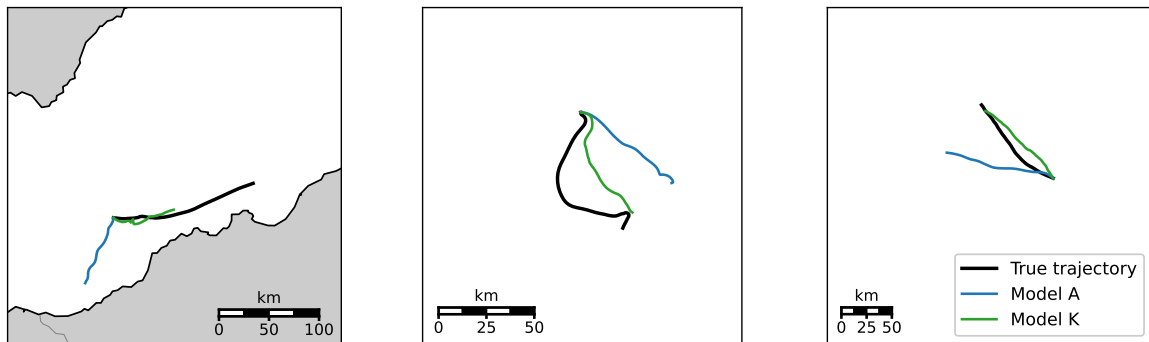

Figure 19: Examples of three observed drifters' trajectories (black), and predicted trajectories using the best physical model (Model A, in blue) and the baseline hybrid model (Model K, in green).
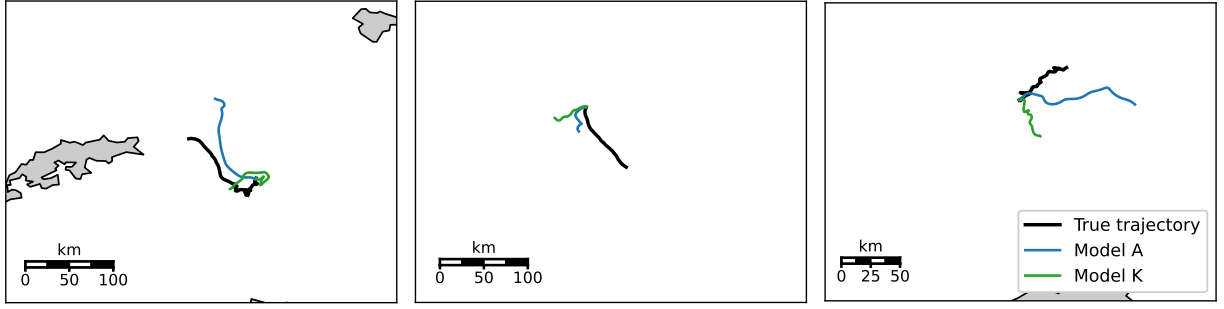
38

Figure 20: Examples of three observed drifters trajectories (black), and predicted trajectory using the best physical model (Model A, in blue) and the baseline hybrid model (Model K, in green). For these trajectories, the data-driven correction does not improve the prediction of the model.

Similar to the challenge encountered with differentiating between models A, B, and C based on visual assessment alone, the performances of the various variations (Models K-P) are also imperceptible through qualitative analysis. An illustrative example of trajectories predicted by all the models is still presented in Figure 21.
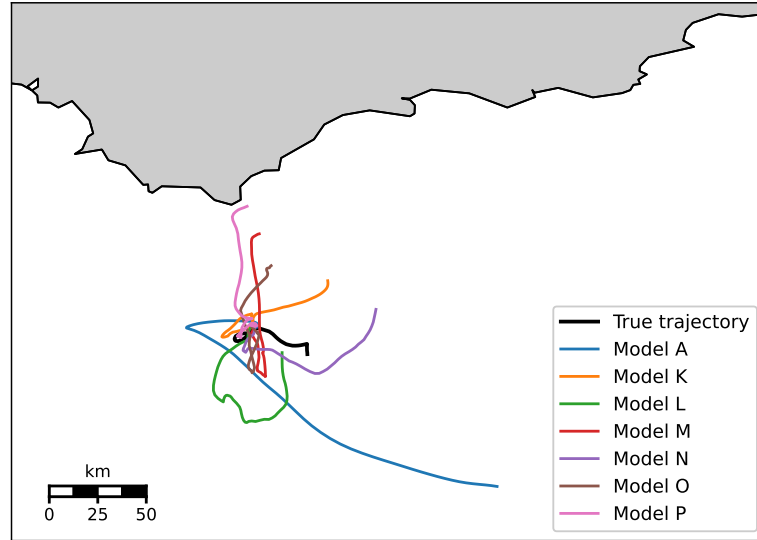
Figure 21: Example of trajectories predicted by the different variations of the hybrid model (Models K-P) in contrast with the predictions of the physical model (Model A) and the true observed trajectories of the drifting buoys. The trajectories obtained vary significantly with the model, although we can note that the use of a data-driven correction tends to improve the prediction. None of the variations of the hybrid model clearly outperforms the others.

As before, to enable a proper and objective comparison, the models are assessed on 100 trajectories from the test set using the metrics described in Section 4.4. The aggregated scores are provided in Table 7. For this part, the models are only tested on the trajectories and not on the probability distributions obtained.

The models are first tested in their ability to accurately predict the next position of the floating object based on its current position. As anticipated, considering the models were trained for this purpose, the incorporation of a data-driven component enhances this prediction. No clear distinction is however made between the different variations of the hybrid model.

Turning to the separation distance d_s, the skill score ssc and the time-averaged distance tad, noticeable improvement is observed when employing a hybrid model. The improvement is less pronounced in the initial hours of prediction but becomes clearer with elapsed time. While differences between models remain minimal, it is noteworthy that the use of historical positional data (Model O) surprisingly exhibits enhanced performance for early predictions (up to 12 hours). Interestingly, for the tested values of context size N and area spanned d, no significant differences were found in the final prediction. This reaffirms the observation made in Section 3.2.1 that the coarse resolution of the data implies that further increasing the number of points in the context does not lead to improved performance. Regrettably, the trajectory-based training tend to diminish the global forecasting performances.

Table 7: Averaged hybrid models performances on the test set (100 trajectories). Bold values represent best performances. Uncertainties represent standard deviations for 10000 bootstrap resamples.

Metric	Time	Model A $u_d = u_O + Au_W$	Model K (hybrid)	Model L (hybrid)	Model M (hybrid)	Model N (hybrid)	Model O (hybrid)	Model P (hybrid)
Number of points in the context	-	-	32	32	64	32	32	32
Context size [km]	-	-	50	100	50	50	50	50
Specificities	-	-	-	-	-	angle correction	historical positional data	trajectory-based loss and training
ds [km] (next point prediction)	-	1.22 ± 0.02	1.00 ± 0.02	1.02 ± 0.02	1.01 ± 0.02	0.99 ± 0.02	1.02 ± 0.02	1.08 ± 0.02
ds [km]	3h	2.9 ± 0.3	2.8 ± 0.4	3.0 ± 0.4	2.9 ± 0.4	2.9 ± 0.4	$\mathbf{1.9 \pm 0.3}$	3.0 ± 0.4
	6h	5.4 ± 0.6	5.4 ± 0.8	5.6 ± 0.8	5.5 ± 0.8	5.5 ± 0.8	$\mathbf{4.6 \pm 0.7}$	5.7 ± 0.8
	12h	11 ± 1	$\mathbf{10 \pm 1}$	$\mathbf{10 \pm 2}$	$\mathbf{10 \pm 1}$	$\mathbf{10 \pm 2}$	$\mathbf{10 \pm 1}$	11 ± 2
	24h	20 ± 2	19 ± 2	$\mathbf{18 \pm 3}$	$\mathbf{18 \pm 3}$	18 ± 3	$\mathbf{18 \pm 3}$	19 ± 3
	48h	38 ± 5	34 ± 5	$\mathbf{32 \pm 5}$	34 ± 5	33 ± 5	33 ± 5	36 ± 5
	72h	55 ± 8	47 ± 7	$\mathbf{44 \pm 7}$	48 ± 7	46 ± 8	49 ± 8	52 ± 8
ssc	3h	0.16 ± 0.04	0.20 ± 0.05	0.20 ± 0.05	0.20 ± 0.05	0.19 ± 0.05	$\mathbf{0.44 \pm 0.06}$	0.20 ± 0.05
	6h	0.19 ± 0.05	0.22 ± 0.05	0.22 ± 0.06	0.20 ± 0.05	0.22 ± 0.05	$\mathbf{0.34 \pm 0.06}$	0.23 ± 0.05
	12h	0.20 ± 0.05	0.25 ± 0.06	0.27 ± 0.06	0.25 ± 0.05	0.25 ± 0.06	$\mathbf{0.30 \pm 0.06}$	0.26 ± 0.06
	24h	0.21 ± 0.05	0.28 ± 0.05	0.29 ± 0.06	0.28 ± 0.05	0.28 ± 0.05	$\mathbf{0.31 \pm 0.06}$	0.29 ± 0.06
	48h	0.24 ± 0.05	0.30 ± 0.06	0.31 ± 0.06	0.32 ± 0.05	$\mathbf{0.33 \pm 0.05}$	0.32 ± 0.06	0.32 ± 0.05
	72h	0.26 ± 0.05	0.32 ± 0.06	0.35 ± 0.06	0.34 ± 0.05	$\mathbf{0.37 \pm 0.06}$	0.34 ± 0.06	0.34 ± 0.05
tad [km/h]	3h	2.0 ± 0.2	1.9 ± 0.3	2.0 ± 0.3	1.9 ± 0.3	1.9 ± 0.3	$\mathbf{1.0 \pm 0.2}$	2.0 ± 0.3
	6h	3.3 ± 0.3	3.2 ± 0.5	3.4 ± 0.5	3.3 ± 0.5	3.3 ± 0.5	$\mathbf{2.4 \pm 0.3}$	3.4 ± 0.5
	12h	5.9 ± 0.6	5.7 ± 0.8	5.8 ± 0.8	5.7 ± 0.8	5.8 ± 0.8	$\mathbf{4.9 \pm 0.7}$	6.1 ± 0.9
	24h	11 ± 1	$\mathbf{10 \pm 1}$	$\mathbf{10 \pm 1}$	$\mathbf{10 \pm 1}$	$\mathbf{10 \pm 1}$	$\mathbf{10 \pm 1}$	11 ± 1
	48h	21 ± 2	19 ± 2	$\mathbf{18 \pm 2}$	$\mathbf{18 \pm 3}$	$\mathbf{18 \pm 3}$	$\mathbf{18 \pm 3}$	20 ± 3
	72h	30 ± 4	26 ± 4	$\mathbf{24 \pm 4}$	26 ± 4	25 ± 4	26 ± 4	28 ± 4

6   Discussion

Despite offering accurate forecasts for the majority of trajectories away from the shores, the physical model encountered notable challenges in correctly predicting trajectories near coastal regions, a phenomenon attributable to the intricate and diverse dynamics prevailing in these areas. Indeed, factors such as the presence of river plumes, coastal fronts, coastal currents, and potential beaching greatly contribute to the complexity of nearshore dynamics [8]. In addition, and despite the correct interpolation of available data, the coarse resolution of the environmental data also remains a limiting factor, preventing the capture of small-scale variations crucial for understanding the dynamics of small drifting objects. This limitation becomes particularly noticeable when considering phenomena like the accumulation in cyclonic eddies at the surface [8], which, despite their impact on the trajectories of drifting objects, remain unresolved even in high-resolution oceanic models.

The coarse resolution of the data imposes a significant constraint not only on the physical model but also on the hybrid model and its data-driven component. This aspect contributes to the observed challenges in achieving separation distances between true and predicted positions within the sub-kilometer range in the initial hour of prediction. Indeed, with a resolution ranging between $1/2°$ and $1/12°$, i.e. which can reach 56km, it appears ambitious to surpass a prediction accuracy of 1 km. Additionally, the non-negligible propagation of errors introduced by the successive iterations of the model is responsible for the large errors encountered after a few hours.

A potential solution for mitigating the challenges imposed by the coarse resolution of the data and the resulting error propagation involves a shift in the methodology employed for trajectory computation. Specifically, the adoption of sequence-to-sequence algorithms could offer a promising solution. By directly predicting entire trajectories with multiple successive positions as input, these algorithms bypass the need for successive model runs based on obtained positions. Alternatively, recurrent neural networks (RNN) or Long Short-Term Memory (LSTM) networks could be leveraged to encode memory and predict successive positions more continuously. Such an approach also holds the promise of capturing complex temporal dependencies more effectively. By encoding memory within the network architecture, these models inherently account for the sequential nature of trajectory data, providing a more comprehensive and accurate prediction mechanism.

A noteworthy alternative for incorporating memory and trajectory-related information into the model also emerges from the performance boost observed with the inclusion of additional information about previous positions, as demonstrated by Model O. The notable improvements highlight the potential importance of temporal context in improving predictions. The efficiency of this modification also implies a potential deficit in the amount of pertinent information fed to the model, explaining the stagnation in performance witnessed with other modifications.

The performances exhibited by Model O also shed light on a potential explanation for the underperformance of Model P, despite the promise of an enhanced understanding of the notion of trajectory. Particularly, it questions the choice of maintaining a consistent context across all computations

within a trajectory. This approximation was rationalized by the high correlation observed between contexts separated by one hour. However, the enhanced performance observed in Model O, where the context from an hour prior is still considered despite this correlation, suggests a reevaluation of this approach. Computing the context dynamically within Model P, allowing it to evolve in response to trajectory evolution, might yield notable performance increases. However, this enhancement comes at the cost of larger computational costs, emphasizing the inherent trade-off between computational efficiency and predictive accuracy in the optimization of trajectory prediction models.

An additional suggestion for improvement of the predictions involves a more judicious selection of the data fed to the model, recognizing that the current sampling methodology could be further optimized. Particularly, a primary challenge faced by the physical model lies in the prediction of trajectories near the coast. This observation advocates for a non-random dataset sampling approach and an increase in the representation of trajectories in close proximity to coastlines, to enhance the ability of the data-driven component to account for these scenarios. The dataset also gathers trajectories from buoys both with and without a drogue. Given the different dynamics associated with these two types of objects, it becomes pertinent to explore the potential benefits of employing separate models for each case. More precisely, considering the targeted floating objects, namely plastic waste, it may be sufficient to exclusively focus on buoys without a drogue, as these more accurately simulate the dynamics of the intended target.

Eventually, note that we concentrate our efforts on developing a model that works on a global scale across the entire globe. This objective necessitates datasets and models that cover oceanic and meteorological predictions on a global scale. However, this ambitious global scope is constrained by the computational challenges associated with maintaining higher resolutions over extensive areas. To optimize computational efficiency, existing oceanic and meteorologic prediction models often resort to lower resolutions, thereby sacrificing the finer details crucial for accurate trajectory predictions. An alternative approach involves narrowing the scope and concentrating efforts on smaller geographic areas characterized by superior data quality and higher resolution, therefore holding the potential for better predictions. Either way, it is necessary to find an appropriate balance between global model aspirations and the imperative for accuracy.

Lastly, and despite the aforementioned challenges, the promising outcomes observed highlight the potential efficacy of employing a hybrid model for predicting the drift of floating objects. The combination of physical and data-driven approaches holds significant potential for addressing the complexities of oceanic drift dynamics.

Conclusion

This work addressed the pressing environmental issue of plastic waste proliferation in oceans, emphasizing the need for accurate modeling and prediction of oceanic drifts of plastic waste. It explored both traditional physical modeling and data-driven approaches for predicting the movement of floating objects at the surface, recognizing the challenges each method presents.

The study established baseline models demonstrating promising outcomes, by integrating both physical and data-driven components. The physical framework alone already provided satisfactory results, despite some notable difficulties in predicting trajectories near coastal regions. The addition of a data-driven correction term to the prediction of the traditional physical model helped increase significantly the forecasting capability of the model, regardless of the limitations caused by the coarse resolution of the environmental data. Proposed improvements included considering an extended spatial and temporal context for the prediction, and the inclusion of the notion of trajectory in the structure of the model. Specifically, the augmentation of the data with additional information on past positions and the historical environmental context demonstrated significant benefits, leading to a notable enhancement in the model's predictive accuracy.

Despite some remaining challenges such as the more judicious selection of the training data as well as their resolution, the promising outcomes obtained underscore the potential efficacy of hybrid models in predicting the drift of floating objects. In the end, this combination of physical and data-driven approaches hold significant promise for addressing the complex dynamics behind the trajectories of floating objects and contributing to plastic pollution mitigation.

References

[1] M. Eriksen, W. Cowger, L. M. Erdle, S. Coffin, P. Villarrubia-Gómez, C. J. Moore, E. J. Carpenter, R. H. Day, M. Thiel, and C. Wilcox, "A growing plastic smog, now estimated to be over 170 trillion plastic particles afloat in the world's oceans—urgent solutions required," *Plos one*, vol. 18, no. 3, p. e0281596, 2023.

[2] A. Anastasopoulou and T. Fortibuoni, "Impact of plastic pollution on marine life in the mediterranean sea," in *Plastics in the Aquatic Environment-Part I: Current Status and Challenges*, pp. 135–196, Springer, 2019.

[3] R. Waring, R. Harris, and S. Mitchell, "Plastic contamination of the food chain: A threat to human health?," *Maturitas*, vol. 115, pp. 64–68, 2018.

[4] M. Carbery, W. O'Connor, and T. Palanisami, "Trophic transfer of microplastics and mixed contaminants in the marine food web and implications for human health," *Environment International*, vol. 115, pp. 400–409, 2018.

[5] S. Bosi, G. Broström, and F. Roquet, "The Role of Stokes Drift in the Dispersal of North Atlantic Surface Marine Debris," *Frontiers in Marine Science*, vol. 8, p. 697430, Aug. 2021.

[6] B. Hackett, Ø. Breivik, and C. Wettre, *Forecasting the Drift of Objects and Substances in the Ocean*, pp. 507–523. Dordrecht: Springer Netherlands, 2006.

[7] R. Stewart, *Introduction to Physical Oceanography*. Texas A&M University, 2004.

[8] E. van Sebille et. al., "The physical oceanography of the transport of floating marine debris," *Environmental Research Letters*, vol. 15, p. 023003, feb 2020.

[9] V. Onink, D. Wichmann, P. Delandmeter, and E. van Sebille, "The role of ekman currents, geostrophy, and stokes drift in the accumulation of floating microplastic," *Journal of Geophysical Research: Oceans*, vol. 124, no. 3, pp. 1474–1490, 2019.

[10] V. de Aguiar, J. Röhrs, A. M. Johansson, and T. Eltoft, "Assessing ocean ensemble drift predictions by comparison with observed oil slicks," *Frontiers in Marine Science*, vol. 10, 2023.

[11] B. Kraft, M. Jung, M. Körner, S. Koirala, and M. Reichstein, "Towards hybrid modeling of the global hydrological cycle," *Hydrology and Earth System Sciences*, vol. 26, no. 6, pp. 1579–1614, 2022.

[12] S. Zhong, K. Zhang, M. Bagheri, J. G. Burken, A. Gu, B. Li, X. Ma, B. L. Marrone, Z. J. Ren, J. Schrier, *et al.*, "Machine learning: new ideas and tools in environmental science and engineering," *Environmental Science & Technology*, vol. 55, no. 19, pp. 12741–12754, 2021.

[13] H. Li, H. Jiao, and Z. Yang, "Ais data-driven ship trajectory prediction modelling and analysis based on machine learning and deep learning methods," *Transportation Research Part E: Logistics and Transportation Review*, vol. 175, p. 103152, 2023.

[14] X. Li, K. Wang, M. Tang, J. Qin, P. Wu, T. Yang, and H. Zhang, "Marine drifting trajectory prediction based on lstm-dnn algorithm," *Wireless Communications and Mobile Computing*, vol. 2022, 2022.

[15] D. Botvynko, C. Granero-Belinchon, S. Van Gennip, A. Benzinou, and R. Fablet, "Deep learning for lagrangian drift simulation at the sea surface," in *ICASSP 2023-2023 IEEE International Conference on Acoustics, Speech and Signal Processing (ICASSP)*, pp. 1–5, IEEE, 2023.

[16] D. Shen, S. Bao, L. J. Pietrafesa, and P. Gayes, "Improving numerical model predicted float trajectories by deep learning," *Earth and Space Science*, vol. 9, no. 9, p. e2022EA002362, 2022.

[17] A. Baier, Z. Boukhers, and S. Staab, "Hybrid physics and deep learning model for interpretable vehicle state prediction," *arXiv preprint arXiv:2103.06727*, 2021.

[18] A. Al-Rabeh, "Estimating surface oil spill transport due to wind in the Arabian Gulf," *Ocean Engineering*, vol. 21, pp. 461–465, July 1994.

[19] A. Al-Rabeh, R. Lardner, and N. Gunay, "Gulfspill Version 2.0: a software package for oil spills in the Arabian Gulf," *Environmental Modelling & Software*, vol. 15, pp. 425–442, June 2000.

[20] M. Leppäranta, *The Drift of Sea Ice*. Karst and Cavernous Rocks in Engineering and Const, Springer, 2005.

[21] T. J. W. Wagner, I. Eisenman, A. M. Ceroli, and N. C. Constantinou, "How winds and ocean currents influence the drift of floating objects," *Journal of Physical Oceanography*, vol. 52, no. 5, pp. 907 – 916, 2022.

[22] M.-S. Chang, "Mass transport in deep-water long-crested random gravity waves," *Journal of Geophysical Research (1896-1977)*, vol. 74, no. 6, pp. 1515–1536, 1969.

[23] G. Stokes, *On the Theory of Oscillatory Waves*. 1880.

[24] M. S. Longuet-Higgins, "Mass transport in water waves," *Philosophical Transactions of the Royal Society of London. Series A, Mathematical and Physical Sciences*, vol. 245, no. 903, pp. 535–581, 1953.

[25] Huang Ne, "Mass transport induced by wave motion," *Journal of Marine Research*, vol. 28, no. 1, pp. 35–50, 1970.

[26] T. van den Bremer and O. Breivik, "Stokes drift," *Philosophical Transactions of The Royal Society A Mathematical Physical and Engineering Sciences*, vol. 376, p. 20170104, 01 2018.

[27] A. Al-Rabeh, "Estimating surface oil spill transport due to wind in the Arabian Gulf," *Ocean Engineering*, vol. 21, pp. 461–465, July 1994.

[28] K. Christensen, Breivik, K.-F. Dagestad, J. Röhrs, and B. Ward, "Short-Term Predictions of Oceanic Drift," *Oceanography*, vol. 31, pp. 59–67, Sept. 2018.

[29] U. Callies, N. Groll, J. Horstmann, H. Kapitza, H. Klein, S. Maßmann, and F. Schwichtenberg, "Surface drifters in the German Bight: model validation considering windage and Stokes drift," *Ocean Science*, vol. 13, pp. 799–827, Sept. 2017.

[30] T. Tamtare, D. Dumont, and C. Chavanne, "Extrapolating eulerian ocean currents for improving surface drift forecasts," *Journal of Operational Oceanography*, vol. 14, pp. 1–15, 09 2019.

[31] T. Tamtare, D. Dumont, and C. Chavanne, "The stokes drift in ocean surface drift prediction," *Journal of Operational Oceanography*, vol. 15, pp. 1–13, 01 2021.

[32] J. Röhrs, K. H. Christensen, L. R. Hole, G. Broström, M. Drivdal, and S. Sundby, "Observation-based evaluation of surface wave effects on currents and trajectory forecasts," *Ocean Dynamics*, vol. 62, pp. 1519–1533, Dec 2012.

[33] J. Roy, "Cozoil: coastal zone oil spill model (for microcomputers). software," tech. rep., Minerals Management Service, Anchorage, AK (USA). Alaska Outer Continental . . . , 1988.

[34] M. De Dominicis, P. Nadia, G. Zodiatis, and R. Archetti, "Medslik-ii, a lagrangian marine oil spill model for short-term forecasting - part 2: Numerical simulations and validations," *Geoscientific Model Development Discussions*, vol. 6, pp. 1999–2043, 03 2013.

[35] M. De Dominicis, S. Falchetti, F. Trotta, N. Pinardi, L. Giacomelli, N. Ernesto, L. Fazioli, R. Sorgente, P. jr, P. Lermusiaux, F. martins, and M. Cocco, "A relocatable ocean model in support of environmental emergencies: The costa concordia emergency case," *Ocean Dynamics*, vol. 64, 04 2014.

[36] A. Berry, T. Dabrowski, and K. Lyons, "The oil spill model oiltrans and its application to the celtic sea," *Marine pollution bulletin*, vol. 64, no. 11, pp. 2489–2501, 2012.

[37] B. Blanke and S. Raynaud, "Kinematics of the pacific equatorial undercurrent: An eulerian and lagrangian approach from gcm results," *Journal of Physical Oceanography*, vol. 27, no. 6, pp. 1038–1053, 1997.

[38] K. Döös, J. Kjellsson, and B. Jönsson, "Tracmass—a lagrangian trajectory model," *Preventive methods for coastal protection: Towards the use of ocean dynamics for pollution control*, pp. 225–249, 2013.

[39] M. Lange and E. Van Sebille, "Parcels v0.9: prototyping a Lagrangian ocean analysis framework for the petascale age," *Geoscientific Model Development*, vol. 10, pp. 4175–4186, Nov. 2017.

[40] P. Delandmeter and E. Van Sebille, "The Parcels v2.0 Lagrangian framework: new field interpolation schemes," *Geoscientific Model Development*, vol. 12, pp. 3571–3584, Aug. 2019.

[41] L.-M. Lebreton, S. Greer, and J. Borrero, "Numerical modelling of floating debris in the world's oceans," *Marine Pollution Bulletin*, vol. 64, pp. 653–661, Mar. 2012.

[42] J. Liu, T. Zhang, G. Han, and Y. Gou, "Td-lstm: Temporal dependence-based lstm networks for marine temperature prediction," *Sensors*, vol. 18, no. 11, p. 3797, 2018.

[43] H.-M. Choi, M.-K. Kim, and H. Yang, "Abnormally high water temperature prediction using lstm deep learning model," *Journal of Intelligent & Fuzzy Systems*, vol. 40, no. 4, pp. 8013–8020, 2021.

[44] J. Park, J. Jeong, and Y. Park, "Ship trajectory prediction based on bi-lstm using spectral-clustered ais data," *Journal of marine science and engineering*, vol. 9, no. 9, p. 1037, 2021.

[45] E. De Bézenac, A. Pajot, and P. Gallinari, "Deep learning for physical processes: Incorporating prior scientific knowledge," *Journal of Statistical Mechanics: Theory and Experiment*, vol. 2019, no. 12, p. 124009, 2019.

[46] Y. Yin, V. Le Guen, J. Dona, E. de Bézenac, I. Ayed, N. Thome, and P. Gallinari, "Augmenting physical models with deep networks for complex dynamics forecasting," *Journal of Statistical Mechanics: Theory and Experiment*, vol. 2021, no. 12, p. 124012, 2021.

[47] D. Dumont, P. Nicot, C. Chavanne, T. Tamtare, D. Bourgault, M. Bandet, S. Senneville, J. Caveen, and U. Neumeier, "Track of GPS very-near surface drifters (2014-2015) in the Estuary and Gulf of St. Lawrence, Canada," 2019. Supplement to: Tamtare, Tamkpanka; Dumont, Dany; Chavanne, Cédric (2019): Extrapolating Eulerian ocean currents for improving surface drift forecasts. Journal of Operational Oceanography, 1-15, https://doi.org/10.1080/1755876X.2019.1661564.

[48] S. Elipot, A. Sykulski, R. Lumpkin, L. Centurioni, and M. Pazos, "A dataset of hourly sea surface temperature from drifting buoys," *Scientific Data*, vol. 9, p. 567, Sep 2022.

[49] N. R. Laboratory, "Global ocean forecast system (gofs) 3.1 [dataset]." Available at `https://www.hycom.org/dataserver/gofs-3pt1/analysis`, 2014–2021.

[50] E. J. Metzger, R. W. Helber, P. J. Hogan, P. G. Posey, P. G. Thoppil, T. l. Townsend, A. J. Wallcraft, O. M. Smedstad, D. S. Franklin, L. Zamudio-Lopez, and M. W. Phelps, "Global ocean forecast system 3.1 validation testing," May 2017.

[51] H. Hersbach, B. Bell, P. Berrisford, G. Biavati, A. Horányi, J. Muñoz Sabater, J. Nicolas, C. Peubey, R. Radu, I. Rozum, D. Schepers, A. Simmons, C. Soci, D. Dee, and J.-N. Thépaut, "Era5 hourly data on pressure levels from 1940 to present. copernicus climate change service (c3s) climate data store (cds)." Accessed on 03.10.2023.

[52] T. Nordam, D. Dunnebier, C. Beegle-Krause, M. Reed, and D. Slagstad, "Impact of climate change and seasonal trends on the fate of arctic oil spills," *Ambio*, vol. 46, 10 2017.

[53] J. Röhrs, K.-F. Dagestad, H. Asbjørnsen, T. Nordam, J. Skancke, C. E. Jones, and C. Brekke, "The effect of vertical mixing on the horizontal drift of oil spills," *Ocean Science*, vol. 14, no. 6, pp. 1581–1601, 2018.

[54] S. Weglarczyk, "Kernel density estimation and its application," *ITM Web of Conferences*, vol. 23, p. 00037, 01 2018.

[55] M. Basyir, M. Nasir, S. Suryati, and W. Mellyssa, "Determination of nearest emergency service office using haversine formula based on android platform," *EMITTER International Journal of Engineering Technology*, vol. 5, pp. 270–278, Jan. 2018.

[56] R. Vortmeyer-Kley, P. Nieters, and G. Pipa, "A trajectory-based loss function to learn missing terms in bifurcating dynamical systems," *Scientific Reports*, vol. 11, p. 20394, Oct 2021.

[57] J. M. Price, M. Reed, M. K. Howard, W. R. Johnson, Z.-G. Ji, C. F. Marshall, N. L. Guinasso, and G. B. Rainey, "Preliminary assessment of an oil-spill trajectory model using satellite-tracked, oil-spill-simulating drifters," *Environmental Modelling Software*, vol. 21, no. 2, pp. 258–270, 2006. Progress in Marine Environmental Modelling.

[58] Y. Liu and R. H. Weisberg, "Evaluation of trajectory modeling in different dynamic regions using normalized cumulative lagrangian separation," *Journal of Geophysical Research: Oceans*, vol. 116, no. C9, 2011.

[59] L. M. Castro-Rosero, I. Hernandez, J. M. Alsina, and M. Espino, "Transport and accumulation of floating marine litter in the black sea: insights from numerical modeling," *Frontiers in Marine Science*, vol. 10, 2023.

[60] I. I, L. Hole, K. L, C. Wettre, and J. Röhrs, "Comparison of operational oil spill trajectory forecasts with surface drifter trajectories in the barents sea," *Journal of Geology Geoscience*, vol. 1, 01 2012.

[61] G. S. Vieira, I. I. Rypina, and M. R. Allshouse, "Uncertainty quantification of trajectory clustering applied to ocean ensemble forecasts," 2020.

[62] J. Urain and J. Peters, "Generalized multiple correlation coefficient as a similarity measurements between trajectories," 2019.

[63] W. Schwartz, "J. e. smith (editor), 'torrey canyon', pollution and marine life (a report by the plymoith laboratory of the marine biological association of the united kingdom). xiv u. 196 s., 39 abb., 27 tab., 29, z. z. farbige tafeln. cambridge 1968: Cambridge university press 55 s," *Zeitschrift für allgemeine Mikrobiologie*, vol. 9, no. 6, pp. 493–493, 1969.

[64] L. T. Malcolm, L. S. Eric, Anderson, T. Isaji, and E. Howlett, "Simulation of the oil trajectory and fate in the arabian gulf from the mina al ahmadi spill," *Marine Environmental Research*, vol. 36, pp. 79–115, 1993.

[65] S. D. Smith and E. G. Banke, "The influence of winds, currents and towing forces on the drift of icebergs," *Cold Regions Science and Technology*, vol. 6, no. 3, pp. 241–255, 1983.

[66] C. Garrett, J. Middleton, M. Hazen, and F. Majaess, "Tidal currents and eddy statistics from iceberg trajectories off labrador," *Science*, vol. 227, no. 4692, pp. 1333–1335, 1985.

[67] P. Daniel, G. Jan, F. Cabioc'h, Y. Landau, and E. Loiseau, "Drift modeling of cargo containers," *Spill Science Technology Bulletin*, vol. 7, no. 5, pp. 279–288, 2002.

[68] T. Akiba, S. Sano, T. Yanase, T. Ohta, and M. Koyama, "Optuna: A next-generation hyperparameter optimization framework," in *Proceedings of the 25th ACM SIGKDD International Conference on Knowledge Discovery and Data Mining*, 2019.

[69] T. J. W. Wagner, R. W. Dell, and I. Eisenman, "An analytical model of iceberg drift," *Journal of Physical Oceanography*, vol. 47, no. 7, pp. 1605 – 1616, 2017.

[70] O. Nesterov, "Consideration of various aspects in a drift study of mh370 debris," *Ocean Science*, vol. 14, no. 3, pp. 387–402, 2018.

A Mathematical derivations: The physics behind the drift of a floating object

A.1 The Ekman currents

The Ekman currents arise from a force balance between the wind shear stress force, the Coriolis force and the water drag. On a more formal note, the ocean is a continuous medium and satisfies the conservation of mass, momentum, and energy. Three forces are important: The wind stress, the friction, and the Coriolis force. These forces must balance for steady flow. In this case, the equations of motion in cartesian coordinates are:

$$0 = \frac{\partial u}{\partial x} + \frac{\partial v}{\partial y} + \frac{\partial w}{\partial z}, \tag{18}$$

$$\frac{\partial u}{\partial t} = -\frac{1}{\rho}\frac{\partial p}{\partial x} + fv + F_x, \tag{19}$$

$$\frac{\partial v}{\partial t} = -\frac{1}{\rho}\frac{\partial p}{\partial y} - fu + F_y, \tag{20}$$

$$\frac{\partial w}{\partial t} = -\frac{1}{\rho}\frac{\partial p}{\partial z} - g, \tag{21}$$

with (u, v, w) the velocity components of the fluid, ρ the water density, p the pressure, $f = 2\Omega \sin\varphi$ the Coriolis factor with Ω the rotation rate of the Earth and φ the latitude, and $F_x = \nu\frac{\partial^2 u}{\partial z^2}$ and $F_y = \nu\frac{\partial^2 v}{\partial z^2}$ the components of the friction force with ν the eddy viscosity. Since there is little variation in these parameters on the scale of an Ekman spiral, and for simplicity, ρ and ν are taken constant.

If one considers a steady-state homogeneous ocean, with an horizontal flow, i.e.

$$\frac{\partial}{\partial t} = \frac{\partial}{\partial x} = \frac{\partial}{\partial y} = \frac{\partial}{\partial z} = 0, \tag{22}$$

these equations can be reduced to :

$$fv = -\nu\frac{\partial^2 u}{\partial z^2}, \tag{23}$$

$$fu = \nu\frac{\partial^2 v}{\partial z^2}. \tag{24}$$

With no shear boundary conditions, this system of equations has the Ekman spiral solution depicted in Figure 1a, here in the case of a southerly wind:

$$u_{\text{Ekman}} = V_0 \exp(az)\cos\left(\frac{\pi}{4} + az\right) \tag{25}$$

$$v_{\text{Ekman}} = V_0 \exp(az)\sin\left(\frac{\pi}{4} + az\right), \tag{26}$$

with $V_0 = \frac{\tau}{\sqrt{\rho^2 f\nu}}$ the current at sea surface (τ being the shear stress), and $a = \sqrt{f/2\nu}$ the rotation of the current with depth.

At the surface, $u_{\text{Ekman}} = V_0 \cos\left(\frac{\pi}{4}\right)$ and $v_{\text{Ekman}} = V_0 \sin\left(\frac{\pi}{4}\right)$, so the surface current is rotated with an angle of $\pi/4 = 45°$ to the right (northern hemisphere) or left (southern hemisphere) of the wind, as it is empirically observed. Note that because the idealized conditions used to derive the Ekman spiral do not perfectly reflect real ocean, wind-induced water movements often differ from theoretical predictions. The angle between the wind and the current can, for instance, be as little as 15 degrees in shallow water, because the depth is not sufficient for the full spiral to form.

A.2   Inertial currents

Mathematically, the inertial currents are obtained by considering the same equations of motion (18)-(21) in the case where no wind forcing term is applied, and without horizontal pressure gradients. The equations of motion become:

$$u_{\text{inertial}} = V \sin(ft), \tag{27}$$

$$v_{\text{inertial}} = V \cos(ft), \tag{28}$$

$$V = u^2 + v^2. \tag{29}$$

These equations are equations for a circle. Even though we obtained the equations for the oscillation presuming frictionless flow, note that friction cannot be entirely disregarded. With time, the oscillations eventually dissipate.

A.3   The geostrophic currents

When frictional forces are negligible, or neglected, the only forces at work are the pressure gradient and the Coriolis force. The equations of motion can be expressed as a simple balance between the two, called the geostrophic balance.

The mathematical formulation follows the same approach as above. Under the assumptions of a steady state, a hydrostatic balance, negligible vertical velocities, and no viscosity (hence no friction), the equations of motion (18)-(21) become

$$fv = \frac{1}{\rho}\frac{\partial p}{\partial x}, \tag{30}$$

$$fu = -\frac{1}{\rho}\frac{\partial p}{\partial y}, \tag{31}$$

$$-g = \frac{1}{\rho}\frac{\partial p}{\partial z}. \tag{32}$$

These equations can be rewritten as follows:

$$u_{\text{geo}} = -\frac{1}{f\rho}\frac{\partial p}{\partial y}; \qquad v_{\text{geo}} = \frac{1}{f\rho}\frac{\partial p}{\partial x} \tag{33}$$

$$p(h) = p_0 + \int_{-h}^{\xi} g(\varphi, z)\rho(z)dz, \tag{34}$$

where $p(h)$ is the pressure at any depth h and ξ is the height of the sea surface relative to a particular level surface coincident with the ocean at rest (called the geoid), corresponding to $z = 0$.

Substituting (34) into (33) we obtain

$$u_{\text{geo}}(h) = -\frac{1}{f\rho}\frac{\partial}{\partial y}\int_{-h}^{0} g(\varphi, z)\rho(z)dz - \frac{g}{f}\frac{\partial \xi}{\partial y}, \tag{35}$$

$$v_{\text{geo}}(h) = \frac{1}{f\rho}\frac{\partial}{\partial x}\int_{-h}^{0} g(\varphi, z)\rho(z)dz + \frac{g}{f}\frac{\partial \xi}{\partial x}. \tag{36}$$

At the surface ($h = 0$), the geostrophic currents are thus

$$u_{\text{geo}} = -\frac{g}{f}\frac{\partial \xi}{\partial y} \qquad \text{and} \qquad v_{\text{geo}} = \frac{g}{f}\frac{\partial \xi}{\partial x}. \tag{37}$$

A.4 Water drag against wind drag: The velocity of a floating object at the surface of the ocean

If we consider only the drag forces associated with the wind and ocean currents resulting from the phenomena described in section 1.1, and neglect other forces acting on a floating object such as the Coriolis force (justified in [21] and [69]), the momentum equation for a drifting object can be written in the form [6][65]:

$$m\frac{d\boldsymbol{v}}{dt} = \boldsymbol{F}_W + \boldsymbol{F}_A, \tag{38}$$

where

$$\boldsymbol{F}_W = \frac{1}{2}\rho_W C_W A_W |\boldsymbol{v}_W - \boldsymbol{v}|(\boldsymbol{v}_W - \boldsymbol{v}), \tag{39}$$

$$\boldsymbol{F}_A = \frac{1}{2}\rho_A C_A A_A |\boldsymbol{v}_A - \boldsymbol{v}|(\boldsymbol{v}_A - \boldsymbol{v}), \tag{40}$$

are the drag forces due to water and air respectively [70], with ρ_W, ρ_A the density of water and air, C_W, C_A drag coefficients for water and air, A_W, A_A the cross-sectional surface areas of the object facing the relative flow of the water and air, and $\boldsymbol{v}_W$ and $\boldsymbol{v}_A$ the velocities of the surface current and the wind respectively.

Under the following assumptions, justified in [69]:

- The acceleration term $m\frac{d\boldsymbol{v}}{dt}$ is neglected because it is much smaller than other terms in the momentum balance

- The object speed $\boldsymbol{v}$ is taken to be much smaller than the surface wind speed $\boldsymbol{v}_A$, i.e. $\boldsymbol{v}_A - \boldsymbol{v} \approx \boldsymbol{v}_A$

- The water drag is calculated using only the ocean current velocity at the surface, ignoring vertical differences. Similarly, at whatever height, the wind felt by the object is estimated to be equal to the surface wind,

equation (38) becomes $\boldsymbol{F}_W + \boldsymbol{F}_A = 0$ and the solution is given by

$$\boldsymbol{v} = \boldsymbol{v}_W + \underbrace{\sqrt{\frac{\rho_A C_A A_A}{\rho_W C_W A_W}}}_{\alpha} \boldsymbol{v}_A, \tag{41}$$

with ρ_W, ρ_A the density of water and air, C_W, C_A drag coefficients for water and air, and A_W, A_A the cross-sectional surface areas of the object facing the relative flow of the water and air.

B   Drifters Trajectories Dataset

Figures 22 and 23 provide a visualization of the validation and test sets used for the development of the model.
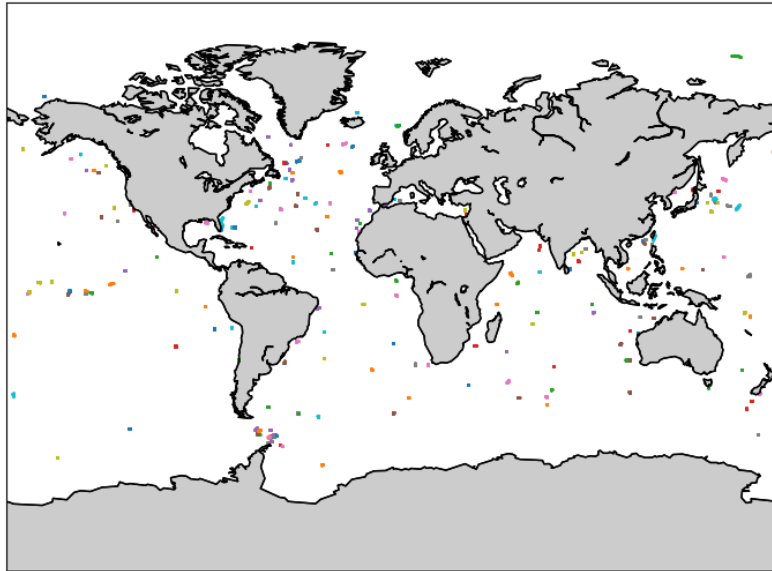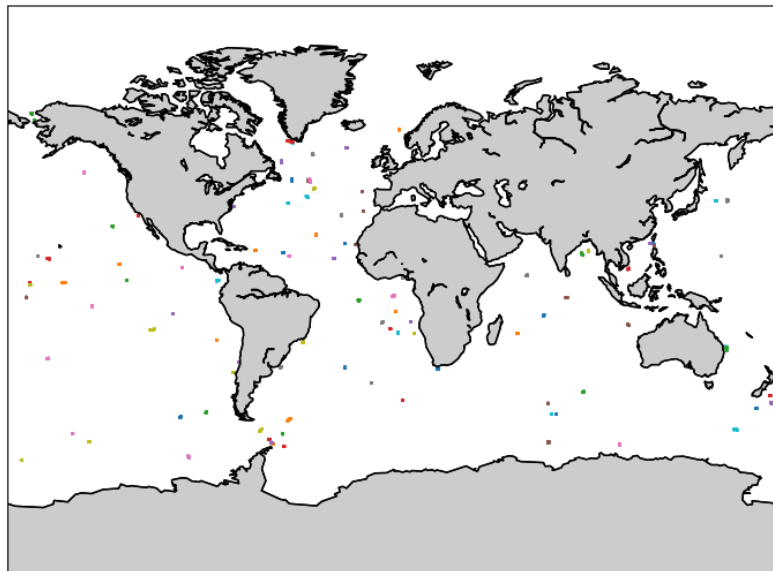

Figure 22: Validation dataset of drifters trajectories.

Figure 23: Test dataset of drifters trajectories.